Model-Based Switching Frequency and Secondary-Side Phase-Shift Angle Matching for Optimizing Efficiency of PV Microconverters

Qianxiang Shen, Qiuye Sun, *Senior Member, IEEE*, Enhui Chu, and Chenghao Sun, *Student Member, IEEE*

***Abstract*—In order to fulfill the requirements of high step-up, wide gain, and high efficiency in photovoltaic (PV) microconverter, an *LCC* resonant converter using a hybrid modulation strategy that combines variable-frequency and secondary-side phase-shift (VF-SSPSM *LCC*) is proposed in this article. By proposing a precise theoretical model, the most appropriate switching frequency (SF) and secondary-side phase-shift angle (SSPSA) that match the steady-state gain under the maximum power point (MPP) of the PV panel are determined, thereby enhancing efficiency while keeping MPP. First, in order to achieve the optimal matching of SF and SSPSA, the working principle of VF-SSPSM *LCC* with PV panel is analyzed, and three operating states are defined according to the difference of resonant tank state. Second, the time-domain state trajectory model is built for three operating states, and the boundary conditions of each state are calculated. Third, the proposed model is employed to conduct loss analysis and derive the theoretical optimal efficiency curve, from which the corresponding SF and SSPSA are determined. Then, a simple efficiency optimization strategy for an MPP steady state of a PV panel is designed. Finally, a prototype is built to verify the accuracy and validity of the proposed theoretical model and optimization strategy.**

***Index Terms*—Efficiency optimization, hybrid modulation, *LCC* resonant converter, photovoltaic (PV) microconverter, secondary-side phase-shift modulation, state trajectory model.**

I. Introduction

PHOTOVOLTAIC (PV) microconverters, as a kind of PV power generation equipment, have significant potential in today's electricity market. Their exceptional reliability, robust environmental adaptability, excellent maximum power point tracking (MPPT) capability, and flexible plugging make them advantageous for enhancing PV penetration [1], [2]. As shown in Fig. 1, these microconverters offer a solution for grid integration of PV modules, allowing building up PV installation starting from a single panel, which can be applied to complex environments, such as buildings, villages, and hills.

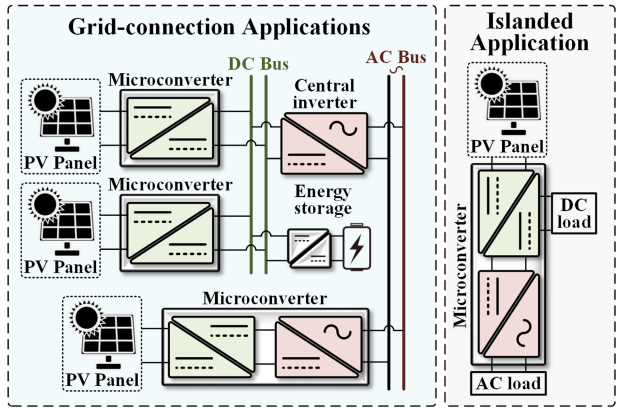

Fig. 1. PV power conditioning systems.

Currently, the output voltage range of a typical PV panel is 10–50 V, while in a standard dc distribution architecture, the bus voltage is 380–400 V, so the microconverters are required to have a high step-up of 40× and a wide gain range of 7.6–40×. Several novel dc–dc converter topologies have been proposed to enhance boost ratio [3], [4] and expand gain range [5], [6]. However, these topologies require additional devices or power transformation stages, which may lead to problems such as large volume, high cost, decreased efficiency, and decreased reliability. Moreover, in the above-mentioned literature, it is also difficult to achieve high step-up and wide gain range at the same time.

An *LCC* resonant converter exhibits exceptional boosting capabilities and has been maturely utilized in ion accelerators [7], high-energy laser technologies [8], X-ray generators [9], and other specialized domains. It is worth noting that an *LCC* resonant converter has exceptional reliability in short-circuit scenarios and is easy to implement soft switching. In addition, the parasitic parameters of the isolation transformer can be fully integrated into the resonant tank to achieve excellent power density. The above-mentioned characteristics align with the requirements of simple structure, high power density, high efficiency, and high reliability. Therefore, an *LCC* resonant converter exhibits potential for utilization as a PV microconverter.

As mentioned above, PV microconverters need both high step-up and wide input voltage range. In order to achieve a

Received 6 June 2024; revised 1 September 2024; accepted 2 October 2024. Date of publication 14 October 2024; date of current version 18 December 2024. This work was supported in part by the National Key Research and Development Program of China under Grant 2018YFA0702200 and in part by the National Natural Science Foundation of China under Grant U20A20190, Grant U23B20118, and Grant 51977028. Recommended for publication by Associate Editor D. Oliveira. *(Corresponding author: Qiuye Sun.)*

The authors are with the College of Information Science and Engineering, Northeastern University, Shenyang 110819, China (e-mail: 2210278@stu.neu.edu.cn; sunqiuye@ise.neu.edu.cn; chuenhui@mail.neu.edu.cn; 1910243@stu.neu.edu.cn).

Color versions of one or more figures in this article are available at https://doi.org/10.1109/TPEL.2024.3480328.

Digital Object Identifier 10.1109/TPEL.2024.3480328

broader gain range in an *LCC* resonant converter, the series resonant inductor should be designed smaller, while the parallel resonant capacitor needs to be designed larger. However, this necessitates a higher switching frequency (SF) to ensure zero voltage switching (ZVS) [10]. Increasing SF will reduce the impedance value of the parallel resonant capacitor, leading to an increase in circulating current, which is detrimental to achieving high efficiency. Consequently, the simultaneous fulfillment of a wide gain range and high efficiency poses a challenge for an *LCC* resonant converter with traditional pulse–frequency modulation (PFM) [11], [12].

In previous studies on resonant converters, a limited number of researchers have employed phase-shifting techniques to reconstruct the relation between SF and gain [13], [14]. Among them, secondary-side phase-shift modulation (SSPSM) stands out as a highly effective method, enabling an *LLC* resonant converter to operate with high efficiency at a series resonant frequency while maintaining a satisfactory gain range [15], [16], [17]. However, the existing studies only apply SSPSM at a fixed SF, which indicates a limitation in the current research. Unlike an *LLC* resonant converter, an *LCC* resonant converter does not operate at the series resonant frequency. As a result, it lacks the apparent advantage of constant frequency operation. It is noteworthy that a hybrid modulation strategy, which combines variable-frequency and SSPSM (VF-SSPSM), can empower an *LCC* resonant converter to possess an exceptionally wide gain range. This characteristic enables VF-SSPSM *LCC* to accommodate most MPPT strategies [18], which confers significant advantages as a PV microconverter.

VF-SSPSM is a suitable modulation method when an *LCC* resonant converter is used as a PV microconverter, which has the following potentials.

1) The gain range can be expanded and the gain upper bound can be improved. The relation between SF and gain can be reconstructed to reduce switching loss.

2) The SSPSA in an *LCC* resonant converter provides an extra degree of freedom, allowing for the optimization of peak values of resonant tank voltage and current in VF-SSPSM *LCC* to reduce core losses and conduction losses.

3) The proposed VF-SSPSM *LCC* model is utilized to compute the minimum SSPSA, thereby providing a possibility for the realization of sensorless synchronous rectification in an *LCC* resonant converter, which can further reduce conduction losses [19], [20].

Therefore, if the SF and SSPSA of an *LCC* resonant converter can be reasonably matched, the operation efficiency can be improved. However, there are the following obstacles to achieve matching: 1) there is no suitable gain model for VF-SSPSM *LCC* to support the theoretical analysis and guide the design; 2) the previous experiments have revealed that the impact of SF and SSPSA on the operational efficiency of an *LCC* resonant converter is nonlinear, and their monotonicity remains uncertain. Therefore, building a high-precision theoretical model of VF-SSPSM *LCC* is a prerequisite to achieve the optimal matching of SF and SSPSA.

There is no rigorous theoretical analysis and mathematical derivation when both variable-frequency and phase-shift modulations are applied to an *LCC* resonant converter. Among many converter modeling methods [21], fundamental harmonic approximation (FHA) is the most prevailing methodology for analyzing resonant converters. The FHA method is employed in [22], [23], and [24] to analyze and model an *LLC* resonant converter, while in [25] and [26], it is used to analyze an *LCC* resonant converter. The accuracy of FHA reaches its peak at series resonant frequency but diminishes as SF deviates from series resonance point [27]. Therefore, due to the fact that an *LCC* resonant converter does not operate in close proximity to the series resonant point, the utilization of FHA will result in a significant error.

The state trajectory method has garnered attention for its ability to provide a more precise description and analysis of the operational process of resonant converters. Initially, the state trajectory method is employed for analyzing and controlling the transient state of the resonant converter due to its ability to accurately describe transient processes. In the early years, Feng et al. [28], [29] have made significant contributions to the field of state trajectory analysis and optimal trajectory control. Subsequently, Zhao et al.'s [30], [31], [32], [33] team has successfully applied the state trajectory method to transient control in an LCC resonant converter. Due to its high precision in describing the operational state of a resonant converter, the state trajectory method has superseded FHA and emerged as the primary analytical approach in an *LCC* resonant converter. Presently, the application of the state trajectory method is no longer confined solely to transient process analysis and control. The state trajectory method is employed in [34] to analyze the steady-state behavior of an *LCC* resonant converter, eliminating the obvious error caused by the analysis using FHA, which introduces a novel perspective for *LCC* resonant converter modeling. In [35], a state trajectory method is employed to conduct steady-state analysis and modeling of an *LCC* resonant converter. By improving the normalization strategy, the established model becomes more intuitive and facilitates analysis and study. However, the current state trajectory analysis and modeling of LCC resonant converters is limited to PFM modes. This model cannot be utilized for the analysis and design of VF-SSPSM *LCC* due to its failure in considering the impact of SSPSA. Therefore, it is necessary to build a state trajectory model of VF-SSPSM *LCC* under full operating conditions, so as to realize the optimal matching of SF/SSPSA under high step-up and wide gain.

In this article, the time-domain state trajectory model of VF-SSPSM *LCC* is established. Based on this model, the effects of SF and SSPSA on the operating efficiency of an *LCC* resonant converter are analyzed. Thus, the feasibility of VF-SSPSM *LCC* to achieve high step-up, wide gain range, and high operation efficiency simultaneously can be verified from the theoretical mechanism level. The main work is as follows.

1) The effect of VF-SSPSM on the operating state of an *LCC* resonant converter is studied and analyzed. The operating range of an *LCC* resonant converter is divided into three different states: Main Energy Delivery (MED) state, Auxiliary Energy Delivery (AED) state, and Lacking Energy Delivery (LED) state. Subsequently, the operation principle of VF-SSPSM *LCC* with PV panel is analyzed.

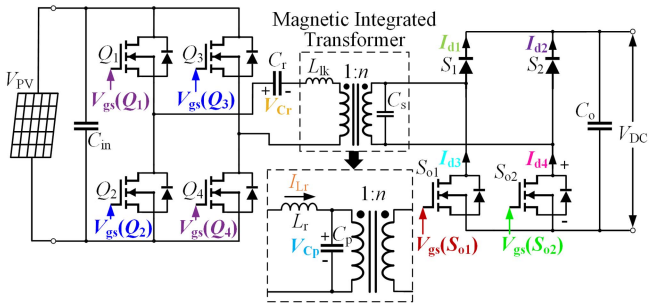

Fig. 2. Topology of a full-bridge *LCC* resonant converter.

2) The trajectory equations are derived separately for three different operating states. Since the state trajectory equation in the LED state is a complex transcendental equation without an analytical solution, the modal analysis conclusion is combined with the linear fitting method to establish the relation between the duration of shunt resonant capacitor short-circuit state and SSPSA in this article, which makes the state trajectory equation of LED state solvable. The boundary conditions for each operating state are derived, ultimately yielding the steady-state model of VF-SSPSM *LCC*.
3) The peak current of the resonant tank in different conditions is analyzed and calculated based on the geometric characteristics of the state trajectory built in this article. Based on this, the loss analysis is implemented, and the matching relation between the optimal efficiency curve of VF-SSPSM *LCC* and SF/SSPSA is derived. Then, based on the optimal matching, the efficiency optimization strategy of VF-SSPSM *LCC* at MPP of the PV panel is designed.

The rest of the article is organized as follows. Section I has an introduction. Section II analyzes the operating states of VF-SSPSM *LCC* with a PV panel. Section III delves deeply into the modeling and analysis of VF-SSPSM *LCC*. Section IV conducts the loss calculation and designs the efficiency optimization strategy of VF-SSPSM *LCC* at the MPP of the PV panel. Section V experimentally verifies the high step-up and wide gain range of VF-SSPSM *LCC*, as well as the optimization for efficiency. Section VI summarizes the conclusion of the study provided.

II. Analysis of Modulating Stages for VF-SSPSM *LCC* With PV Panel

The topology of a full-bridge *LCC* resonant converter operating in the VF-SSPSM mode is shown in Fig. 2. The output port is connected to a dc bus with a fixed output voltage and the input is linked to the PV panel's output port. The primary side consists of MOSFETs Q_1, Q_2, Q_3, and Q_4, while the secondary side comprises diodes S_1, S_2 and MOSFETs S_{o1}, S_{o2}, which can realize phase-shift modulation. The transformer in this topology can be designed using magnetic integration technology, allowing the leakage inductance L_{lk} to serve as the resonant inductor L_r and the equivalent self-capacitance C_s to serve as the parallel

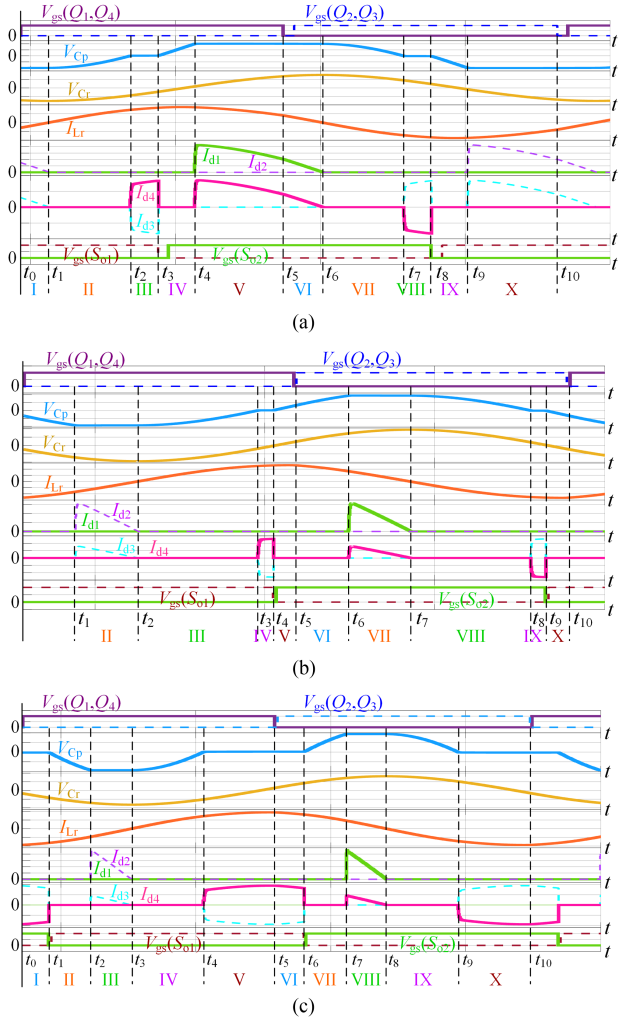

Fig. 3. Typical waveforms of each operating state. (a) MED state. (b) AED state. (c) LED state.

resonant capacitor C_p. All resonance parameters are equivalent to primary side, where $L_r = L_{lk}$ and $C_p = n^2 C_s$. Thus, only one independent resonant element, series resonant capacitor C_r, is needed.

An *LCC* resonant converter is connected to the constant-voltage dc bus via the filter capacitor C_o. By controlling SF and SSPSA, an *LCC* resonant converter can deliver a controllable current I_o to dc bus. The operating characteristics of an *LCC* resonant converter change with SF and SSPSA, leading to different analysis and modeling methods. By summarizing the evolution law of modulating stages during changes in SF and SSPSA, it is observed that the entire operating range of an *LCC* resonant converter can be categorized into three distinct operating states based on the differences of modulating stages. For the sake of facilitating subsequent discussions, these three typical operating states are referred as MED state, AED state, and LED state. The waveform diagrams illustrating these three operating states are presented in Fig. 3.

In Fig. 3, an operation cycle of VF-SSPSM *LCC* is divided into ten stages as I–X. $V_{gs}(\cdot)$ is the waveform of switching

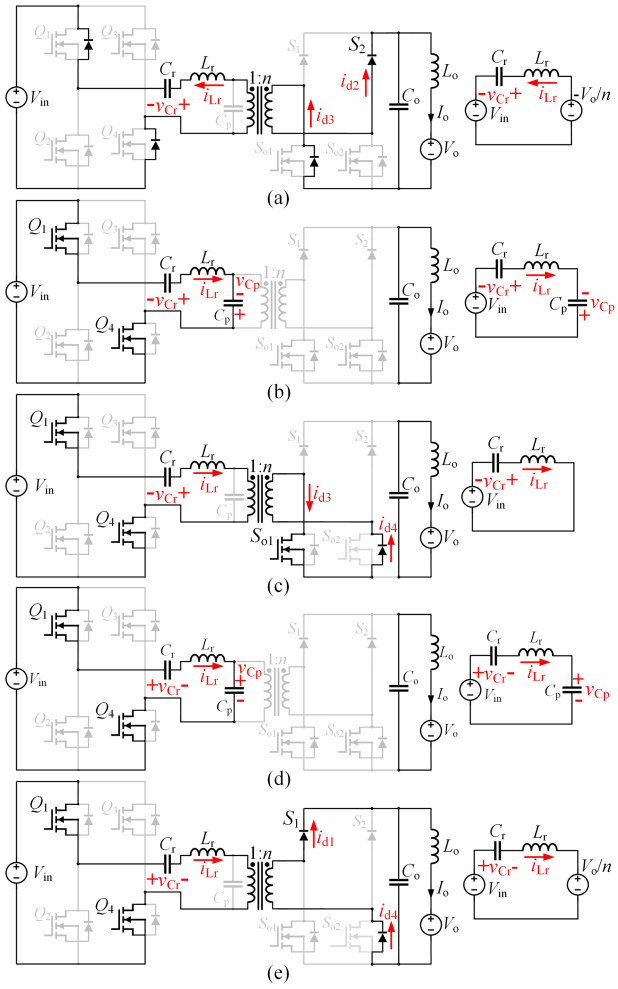

Fig. 4. Equivalent circuits for each operation stage of VF-SSPSM *LCC* under MED state. (a) Stage I. (b) Stage II. (c) Stage III. (d) Stage IV. (e) Stage V.

pulse signal, while V_{Cp}, V_{Cr}, and I_{Lr} in Fig. 3 are the voltage and current waveforms on the resonant element of the resonant tank. In addition, I_{d1}–I_{d4} refer to the current waveforms flowing through S_1, S_2, S_{o1}, and S_{o2}. To generate state trajectories for various operating states, it is imperative to formulate distinct state equations for each modulating stage. The analysis process of each stage under different operating states is partially repetitive. Therefore, this section focuses on a detailed analysis of the MED state. By comparing the key waveforms of MED, AED, and LED states in Fig. 3, it can be found that the key factor to distinguish different operating states is the voltage state on C_{p} when MOSFETs of primary side act. When the MOSFETs act, if V_{Cp} is clamped by output voltage, the *LCC* resonant converter is in the MED state. If C_{p} is being charged, the *LCC* resonant converter is in the AED state. If V_{Cp} is equal to 0, the *LCC* resonant converter is in the LED state.

The equivalent circuits of VF-SSPSM *LCC* at each operation stage are plotted in Fig. 4 using MED state as an example, where the instantaneous polarity of the voltage and the instantaneous direction of current are marked, corresponding to the typical waveform in Fig. 3(a). According to Figs. 3 and 4, the voltage and current state of each operation stage is analyzed, and the trajectory equations are subsequently formulated as follows.

A. MED Operating State

1) Stage I: Combined with Figs. 3(a) and 4(a), the voltage and current statuses of this stage are analyzed. At t_0, the negative resonant current $i_{\mathrm{Lr}}(t_0)$ is conducted through the reverse diode, while the secondary-side current flows into the bus via switches S_{o1} and S_2, and the equivalent output voltage is $-V_o/n$. The resonant tank in this stage consists of C_{r} and L_{r}, the equivalent impedance is $Z_0 = \sqrt{L_r/C_r}$, and the resonant angular frequency is $\omega_0 = 1/\sqrt{L_r \cdot C_r}$. The voltage of C_{p} is clamped in this stage, and power is transmitted to the dc bus until $i_{\mathrm{Lr}}(t)$ reaches 0. At that point, the body diode in the primary side is turned OFF, while Q_1 and Q_4 are turned ON at zero voltage, and the circuit enters the next stage. The state equations of the resonant tank in stage I are as follows:

$$\begin{cases} \frac{dv_{C\mathrm{r}}(t)}{dt} = \frac{i_{Lr}(t)}{C_r} \\ \frac{di_{Lr}(t)}{dt} = \frac{-v_{C\mathrm{r}}(t)+V_{\mathrm{in}}+V_o/n}{L_r}. \end{cases} \tag{1}$$

By substituting the initial state $t = t_0$ into the differential equations, the special solution of (1) can be obtained as

$$\begin{cases} v_{C\mathrm{r}}(t) = i_{Lr}(t_0)Z_0 \sin[\omega_0(t-t_0)] \\ \qquad + [v_{C\mathrm{r}}(t_0) - V_{\mathrm{in}} - V_o/n]\cos[\omega_0(t-t_0)] + V_{\mathrm{in}} + V_o/n \\ i_{Lr}(t) = i_{Lr}(t_0)\cos[\omega_0(t-t_0)] \\ \qquad - [v_{C\mathrm{r}}(t_0) - V_{\mathrm{in}} - V_o/n]\sin[\omega_0(t-t_0)]/Z_0. \end{cases} \tag{2}$$

According to (2), the trajectory equation of stage I can be obtained as

$$\begin{aligned} &i_{Lr}^2(t)Z_0^2 + [v_{C\mathrm{r}}(t) - V_{\mathrm{in}} - V_o/n]^2 = i_{Lr}^2(t_0)Z_0^2 \\ &\quad + [v_{C\mathrm{r}}(t_0) - V_{\mathrm{in}} - V_o/n]^2. \end{aligned} \tag{3}$$

2) Stage II: In Fig. 4(b), Q_1 and Q_4 are turned ON when $i_{\mathrm{Lr}}(t)$ zero crossing occurs, leading to a continuous increase in $i_{\mathrm{Lr}}(t)$. At this time, the resonant tank consists of C_{r}, L_{r}, and C_{p}, and the voltage on C_{p} rises from $-V_o/n$ until it is equal to 0 and enters the next stage. The energy transfer between the primary side and the secondary side is absent in this stage, and the equivalent impedance is $Z_1 = \sqrt{L_r(C_r + C_p)/(C_rC_p)}$ while the resonant angular frequency is $\omega_1 = \sqrt{(C_r + C_p)/(L_rC_rC_p)}$. The state equations for the resonant tank in stage II are as follows:

$$\begin{cases} \frac{d[v_{C\mathrm{r}}(t)+v_{Cp}(t)]}{dt} = i_{Lr}(t)\frac{C_r+C_p}{C_rC_p} \\ \frac{di_{Lr}(t)}{dt} = \frac{-v_{C\mathrm{r}}(t)-v_{Cp}(t)+V_{\mathrm{in}}}{L_r}. \end{cases} \tag{4}$$

By substituting the initial state $t = t_1$ into the differential equations, the special solution of (4) can be obtained as

$$\begin{cases} v_{Cr}(t) + v_{Cp}(t) = i_{Lr}(t_1)Z_1 \sin[\omega_1(t-t_1)] \\ \quad +[v_{Cr}(t_1) + v_{Cp}(t_1) - V_{in}]\cos[\omega_1(t-t_1)] + V_{in} \\ i_{Lr}(t) = i_{Lr}(t_1)\cos[\omega_1(t-t_1)] \\ \quad -[v_{Cr}(t_1) + v_{Cp}(t_1) - V_{in}]\sin[\omega_1(t-t_1)]/Z_1. \end{cases} \tag{5}$$

According to (5), the trajectory equation of stage II is

$$i_{Lr}^2(t)Z_1^2 + [v_{Cr}(t) + v_{Cp}(t) - V_{in}]^2 = i_{Lr}^2(t_1)Z_1^2 + [v_{Cr}(t_1) + v_{Cp}(t_1) - V_{in}]^2. \tag{6}$$

3) Stage III: In Fig. 4(c), when the voltage over C_p decreases to 0, $i_{Lr}(t)$ is positive. The drive signal of S_{o1} is in a high level state, and the negative voltage applied to S_{o1} disappears. The loop formed by S_{o1} and S_{o2} short-circuits C_p in this stage, causing the voltage to remain at 0 until S_{o1} is turned OFF. Subsequently, the circuit transitions into the next stage. The resonant tank currently comprises C_r and L_r, with no energy transfer occurring between primary and secondary sides. Similarly, the trajectory equation of stage III can be derived by conducting an analysis on the resonant tank

$$i_{Lr}^2(t)Z_0^2 + [v_{Cr}(t) - V_{in}]^2 = i_{Lr}^2(t_2)Z_0^2 + [v_{Cr}(t_2) - V_{in}]^2. \tag{7}$$

4) Stage IV: In Fig. 4(d), when S_{o1} is turned OFF, C_p is charged by $i_{Lr}(t)$ until v_{Cp} reaches V_o/n, at which point the *LCC* resonant converter transitions into the next stage. The equivalent circuit of this stage is identical to that of stage II. According to (4), the trajectory equation for stage IV can be derived as

$$i_{Lr}^2(t)Z_1^2 + [v_{Cr}(t) + v_{Cp}(t) - V_{in}]^2 = i_{Lr}^2(t_3)Z_1^2 + [v_{Cr}(t_3) + v_{Cp}(t_3) - V_{in}]^2. \tag{8}$$

5) Stage V: In Fig. 4(e), the voltage of C_p is clamped at V_o/n when v_{Cp} rises to V_o/n. At this time, S_1 and S_{o2} are turned ON, while the *LCC* resonant converter continuously supplies power to dc bus until Q_1 and Q_4 are turned OFF, transitioning the circuit into its subsequent stage. The resonant tank in this stage consists of C_r and L_r, and the trajectory equation of stage V can be derived through a state analysis of the resonant tank

$$i_{Lr}^2(t)Z_0^2 + [v_{Cr}(t) - V_{in} + V_o/n]^2 = i_{Lr}^2(t_4)Z_0^2 + [v_{Cr}(t_4) - V_{in} + V_o/n]^2. \tag{9}$$

B. AED Operating State

1) Stage I: At t_0, a negative resonant current $i_{Lr}(t_0)$ flows through the reverse diode. Since the voltage on C_p does not reach $-V_o/n$ at this stage, $i_{Lr}(t)$ continues to charge C_p. Energy transfer between the primary and secondary sides is absent until the voltage on C_p reaches $-V_o/n$ and transitions into the next stage. At this time, the resonant tank consists of C_r, L_r, and C_p, and the trajectory equation can be derived as

$$i_{Lr}^2(t)Z_1^2 + [v_{Cr}(t) + v_{Cp}(t) - V_{in}]^2 = i_{Lr}^2(t_0)Z_1^2 + [v_{Cr}(t_0) + v_{Cp}(t_0) - V_{in}]^2. \tag{10}$$

2) Stages II–V: In Fig. 3(b), it can be observed that the waveform characteristics of stages II–V in the AED state exhibit similarities to those of stages I–IV in the MED state, allowing for analysis through analogy.

The analysis of the waveform in Fig. 3(b) reveals distinct differences between the stages of AED and MED states. 1) In MED state, the clamping state of C_p voltage is categorized into two stages: I and V. However, in the AED state, the clamping state of C_p voltage solely exists in stage II. 2) In MED state, C_p undergoes charging and discharging processes in stages II and IV, with an absolute voltage increment $-V_o/n$. On the other hand, in AED state, C_p is charged and discharged in stages I, III, and V; however, the voltage increment on C_p in stages I and V is unknown.

C. LED Operating State

1) Stage I: At t_0, a negative resonant current $i_{Lr}(t_0)$ flows through the reverse diode. Since S_{o2} is ON at this time, C_p is in a short-circuit state with a voltage of 0 on it, until S_{o2} is turned OFF and enters the next stage. The resonant tank in this stage consists of C_r and L_r, and the trajectory equation can be derived through a state analysis of the resonant tank

$$i_{Lr}^2(t)Z_0^2 + [v_{Cr}(t) - V_{in}]^2 = i_{Lr}^2(t_0)Z_0^2 + [v_{Cr}(t_0) - V_{in}]^2. \tag{11}$$

2) Stages II–V: In Fig. 3(c), it can be observed that the waveform characteristics of stages II–V in the LED state exhibit similarities to those of stages I–IV in the AED state, allowing for analysis through analogy.

The analysis of the waveform in Fig. 3(c) reveals distinct differences between the stages of LED, AED, and MED states. The short-circuit state of C_p only occurs in one stage under MED and AED states, whereas under LED state, the short-circuit state of C_p is divided and appears in both I and V stages.

D. Operation Principle of VF-SSPSM LCC With PV Panel

The PV panel used in this article is integrated with MPT15-150 produced by PowerFilm, and its *I–V* curve under full sun is shown in Fig. 5(a). In this figure, V_{pv} and I_{pv} are the output voltage and current of the PV panel, while V_o is the output voltage of the PV microconverter. Since the output voltage of microconverter is fixed, the output power of the PV panel is only related to the output current of microconverter. The output power of the PV panel can be adjusted by controlling the output current of microconverter to realize MPPT. The operation principle of PV microconverter is described as follows, based on the output current characteristic curve of VF-SSPSM *LCC*.

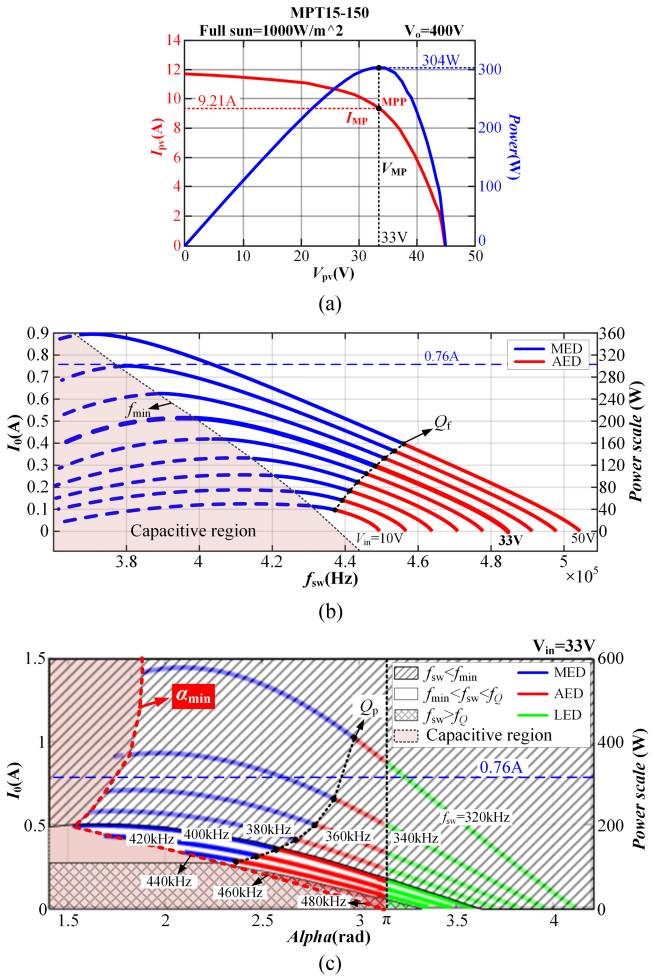

Fig. 5. PV *I–V* curve versus *LCC* resonant converter output current characteristics. (a) PV *I–V* curve. (b) Frequency characteristic curve. (c) Phase-shifting characteristic curve.

When the secondary-side phase shift is not considered, the frequency characteristic curves of an *LCC* resonant converter with different input voltages $V_{\rm in}$ are depicted in Fig. 5(b). By analyzing the phase relationship between voltage and current in resonant tank, it can be found that the capacitive working area of an *LCC* resonant converter is shown as the shaded area in Fig. 5(b), and the capacitive working area and inductive working area are just divided by the inflection point of this series of characteristic curves. It is necessary for $f_{\rm sw}$ to exceed a minimum SF $f_{\rm min}$ since operating in capacitive working area results in hard switching. The blue segment is the characteristic curve of MED state, while the red segment is that of AED state. The intersection of these two segments is $Q_{\rm f}$, and SF at this point is f_Q, which signifies the critical frequency between MED and AED state.

The phase-shifting characteristic curves in Fig. 5(c) are obtained by varying SF while keeping the input voltage $V_{\rm in}$ fixed during the modulation of VF-SSPSM *LCC*. It can be seen that by appropriately setting SSPSA of the *LCC* resonant converter, the inductive region exists even in the slash drawing region of Fig. 5(c) ($f_{\rm sw} < f_{\rm min}$). However, the set SSPSA cannot be too small because if the SSPSA is smaller than $\alpha_{\rm min}$, then the *LCC* resonant converter will enter a capacitive working area, such as the red shaded area in Fig. 5(c). Therefore, a curve can be obtained by concatenating $\alpha_{\rm min}$ at different switching frequencies, and the left side of this curve is a capacitive region and the right side is an inductive region. In this way, compared with PFM, *LCC* resonant converter can operate at a lower SF and achieve a wider gain range.

The blue segment in Fig. 5(c) is the phase-shifting characteristic curve of the MED state, while the red segment is that of the AED state and the green segment is that of the LED state. The transition point of the operating mode from MED to AED in Fig. 5(c) is $Q_{\rm p}$. The phase-shift angle α at this point is α_Q, representing the SSPSA of the operating mode transition. The transition point of AED and LED states remains fixed at $\alpha = \pi$.

In Fig. 5(a), there are $V_{\rm pv} = 33$ V and $I_{\rm pv} = 9.21$ A at the MPP of the PV panel. The output voltage of the microconverter connected to the PV panel is constant at 400 V. According to the power conservation, the output current of the microconverter should be 0.76 A. In Fig. 5(b), microconverter fails to deliver a current of 0.76 A when the input voltage is 33 V, solely relying on PFM operation. However, by employing VF-SSPSM, this can be easily accomplished, and the steady-state performance can be optimized by choosing different SF/SSPSA pairs, as depicted in Fig. 5(c). It can be seen that VF-SSPSM has a significant effect on widening the gain range of *LCC* resonant converter.

III. VF-SSPSM *LCC* State Trajectory Modeling

Based on the stages analysis conclusion from the previous section, it is necessary to construct VF-SSPSM *LCC* state trajectory models for different operating conditions due to variations in stages and resulting differences in state trajectories. The output current ripple is disregarded in the state trajectory model construction, as the output is supported by the substantial bus voltage and the large capacitance and inductance of the output filter. The excitation inductance of the isolation transformer can be disregarded during state analysis due to the minimal excitation current present in the *LCC* resonant converter. The total voltage V_{Crp} across $C_{\rm p}$ and $C_{\rm r}$, as well as the current I_{Lr} flowing through $L_{\rm r}$, are considered as two state variables of the state trajectory. This allows for uniform and continuous changes in the state variables of each stage, facilitating easier calculation and analysis. Furthermore, the state variables need to be normalized in order to enhance the generality and regularity of the model, ensuring fixed center coordinates of the state trajectory and making the characteristics of the trajectory more prominent. The normalization criteria are as follows:

$$\begin{cases} V_N = V/V_{\rm in} \\ I_N = I \cdot Z_0/V_{\rm in} \end{cases} \tag{12}$$

where V and I are the voltage and current values to be normalized, while the voltage and current values after normalization are $V_{\rm N}$ and $I_{\rm N}$. In the following, $V_{Crp\rm N}$ and $I_{Lr\rm N}$ are the normalized values of V_{Crp} and I_{Lr}.

A. MED Operating State

The initial states of stages I–V in Fig. 3(a) need to be calculated first in order to establish the state trajectory model for the MED state. The trajectory equations of each stage, as presented in (3), (6), (7), (8), and (9), are derived based on the stages analysis results discussed in Section II. It should be noted that the switching point between adjacent stages corresponds to the intersection of their respective trajectories. Consequently, these intersection points can be determined by solving the simultaneous trajectory equations. As the trajectory equations for each stage involve two unknowns, the initial value of resonant voltage $V_{Cr\mathrm{p}0}$ and the initial value of resonant current I_{Lr0}, it is evident that a solution cannot be obtained solely through simultaneous trajectory equations. Additional equation relations pertaining to these unknowns must be established.

After re-examining Fig. 3(a), the following characteristics can be observed from the waveform: In stages I and V, energy is transferred from the primary side to the secondary side while the energy in C_p remains constant. In stages II and IV, energy exchange occurs solely between resonant tank and PV panel. During stage III, C_p is short-circuited and the energy is exchanged only between resonant tank and PV panel. According to charge conservation, the following equation is obtained:

$$\Delta Q = nI_o \cdot 0.5T_\mathrm{sw} = \int_{t_0}^{t_1} |i_{Lr}(t)|\,dt + \int_{t_4}^{t_5} |i_{Lr}(t)|\,dt \quad (13)$$

where T_sw is the switching period and ΔQ is the amount of transferred charge, so the relation is as follows:

$$\Delta V_{Cr} = \frac{nI_o}{2C_r f_\mathrm{sw}}. \quad (14)$$

The total voltage increment over C_r during stages I and V is $\Delta V_{Cr} = |V_{Cr}(t_1) - V_{Cr}(t_0)| + |V_{Cr}(t_5) - V_{Cr}(t_4)|$. Furthermore, due to the relation $V_{Cr}(t_0) = -V_{Cr}(t_5)$, it can be concluded that

$$V_{Cr}(t_1) + V_{Cr}(t_4) = -\frac{nI_o}{2C_r f_\mathrm{sw}}. \quad (15)$$

The resonant tank in stages II and IV consists of three components. In each stage, the voltage increment on C_p is V_o/n. Taking stage II as an example, it has

$$\begin{cases} \Delta V_{Cp} = \frac{1}{C_p}\int_{t_1}^{t_2} i_{Lr}(t)dt = \frac{V_o}{n} \\ \Delta V_{Cr} = \frac{1}{C_r}\int_{t_1}^{t_2} i_{Lr}(t)dt = V_{Cr}(t_2) - V_{Cr}(t_1). \end{cases} \quad (16)$$

Eliminate the current integral term in (16)

$$V_{Cr}(t_2) - V_{Cr}(t_1) = \frac{C_p V_o}{nC_r}. \quad (17)$$

Similarly, in stage IV, the following equation holds:

$$V_{Cr}(t_4) - V_{Cr}(t_3) = \frac{C_p V_o}{nC_r}. \quad (18)$$

Section II mentions the existence of α_min for VF-SSPSM *LCC*. The absolute phase-shift angle α_abs is defined as the actual phase lag between S_o1 and S_o2 with respect to Q_2 and Q_1. In Fig. 6, α_min, α_abs, and α_rel are marked. Here, α_min is determined by the inductive area, α_abs is the phase angle at which $V_\mathrm{gs}(S_\mathrm{o2})$ lags $V_\mathrm{gs}(Q_1, Q_4)$, and α_rel is the phase angle corresponding to stage III. Stage III of the MED state is influenced by both α_abs and α_min, as depicted in Fig. 6.

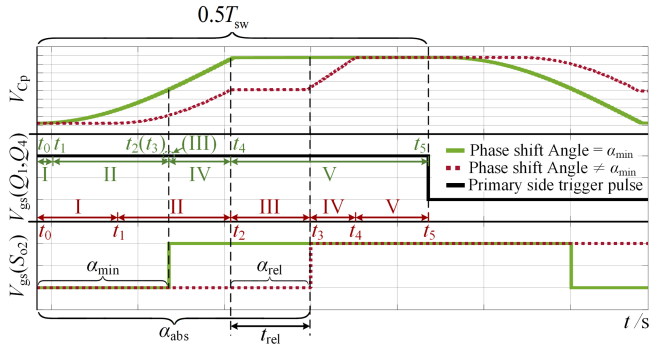

Fig. 6. Analysis of SSPSA under MED state.

In Fig. 6, the green and red curves represent SSPSA equal to or greater than α_min, respectively. The curves in three coordinate systems from top to bottom in Fig. 6 depict the voltage V_{Cp} of C_p, the drive signal $V_\mathrm{gs}(Q_1)$ of Q_1, and the drive signal $V_\mathrm{gs}(S_\mathrm{o2})$ of S_o2. According to the green curve, when $\alpha_\mathrm{abs} = \alpha_\mathrm{min}$, the duration of stage III is zero, the short-circuit state of C_p does not occur, and the *LCC* resonant converter operates in the PFM mode. When $\alpha_\mathrm{abs} > \alpha_\mathrm{min}$, as indicated by the red curve in Fig. 6, the duration of stage III is greater than zero. To facilitate trajectory analysis and formula derivation, the relative phase-shift angle α_rel is defined as follows:

$$\alpha_\mathrm{rel} = 2\pi\frac{t_\mathrm{rel}}{T_\mathrm{sw}} \quad (t_\mathrm{rel} = t_3 - t_2). \quad (19)$$

The duration of stage III, denoted as t_rel, is used to derive the following equations for stage III:

$$\begin{cases} V_{Cr}(t_3) = I_{Lr}(t_2)Z_0\sin(\omega_0 t_\mathrm{rel}) \\ \qquad + [V_{Cr}(t_2) - V_\mathrm{in}]\cos(\omega_0 t_\mathrm{rel}) + V_\mathrm{in} \\ I_{Lr}(t_3) = I_{Lr}(t_2)\cos(\omega_0 t_\mathrm{rel}) \\ \qquad - [V_{Cr}(t_2) - V_\mathrm{in}]\sin(\omega_0 t_\mathrm{rel})/Z_0. \end{cases} \quad (20)$$

The current state involves five equality relations in (15), (17), (18), and (20) with six unknowns, necessitating an additional equality relation. In order to avoid introducing additional unknowns, the state trajectory equation for the time period t_1-t_2 is introduced. This is because at t_1, the resonant tank current I_Lr is 0 and the voltage at C_p is $-V_o/n$, while at t_2, the voltage at C_p becomes 0. The following equation can be obtained by simplifying (6):

$$I_{Lr}^2(t_2)Z_1^2 + [V_{Cr}(t_2) - V_\mathrm{in}]^2 = [V_{Cr}(t_1) - V_o/n - V_\mathrm{in}]^2. \quad (21)$$

The equations for solving state trajectory nodes under MED state can be derived by normalizing (15), (17), (18), (20),

and (21)

$$\begin{cases} V_{C\mathrm{rpN}}(t_1)+V_{C\mathrm{rpN}}(t_4)=-\frac{nI_o}{2C_r f_{\mathrm{sw}} V_{\mathrm{in}}} \\ V_{C\mathrm{rpN}}(t_2)-V_{C\mathrm{rpN}}(t_1)=\frac{C_p V_o}{nC_r V_{\mathrm{in}}}+V_o/n \\ V_{C\mathrm{rpN}}(t_4)-V_{C\mathrm{rpN}}(t_3)=\frac{C_p V_o}{nC_r V_{\mathrm{in}}}+V_o/n \\ V_{C\mathrm{rpN}}(t_3)-1=I_{LrN}(t_2)\sin(\omega_0 t_{\mathrm{rel}}) \\ \qquad\qquad +\left[V_{C\mathrm{rpN}}(t_2)-1\right]\cos(\omega_0 t_{\mathrm{rel}}) \\ I_{LrN}(t_3)=I_{LrN}(t_2)\cos(\omega_0 t_{\mathrm{rel}}) \\ \qquad\qquad -\left[V_{C\mathrm{rpN}}(t_2)-1\right]\sin(\omega_0 t_{\mathrm{rel}}) \\ I_{LrN}^2(t_2)\frac{Z_1^2}{Z_0^2}+\left[V_{C\mathrm{rpN}}(t_2)-1\right]^2=\left[V_{C\mathrm{rpN}}(t_1)-1\right]^2. \end{cases} \tag{22}$$

The independent variables in this equation set are the modulation-related variables f_{sw} and α_{rel}. The dependent variables are the current and voltage of the resonant tank. The solution to (22) can be expressed as follows:

$$\begin{cases} V_{C\mathrm{rpN}}(t_1)=F_{MED-Vt1}(C_r,C_p,L_r,V_{\mathrm{in}},V_o,I_o,n,f_{\mathrm{sw}},t_{\mathrm{rel}}) \\ V_{C\mathrm{rpN}}(t_2)=F_{MED-Vt2}(C_r,C_p,L_r,V_{\mathrm{in}},V_o,I_o,n,f_{\mathrm{sw}},t_{\mathrm{rel}}) \\ V_{C\mathrm{rpN}}(t_3)=F_{MED-Vt3}(C_r,C_p,L_r,V_{\mathrm{in}},V_o,I_o,n,f_{\mathrm{sw}},t_{\mathrm{rel}}) \\ V_{C\mathrm{rpN}}(t_4)=F_{MED-Vt4}(C_r,C_p,L_r,V_{\mathrm{in}},V_o,I_o,n,f_{\mathrm{sw}},t_{\mathrm{rel}}) \\ I_{LrN}(t_2)=F_{MED-It2}(C_r,C_p,L_r,V_{\mathrm{in}},V_o,I_o,n,f_{\mathrm{sw}},t_{\mathrm{rel}}) \\ I_{LrN}(t_3)=F_{MED-It3}(C_r,C_p,L_r,V_{\mathrm{in}},V_o,I_o,n,f_{\mathrm{sw}},t_{\mathrm{rel}}). \end{cases} \tag{23}$$

The complete expression of the solution is not provided due to spatial limitations. The solutions for the six unknowns are dependent on f_{sw} and α_{rel}, while other trajectory parameters can be derived from these six node states. According to the conclusion drawn in Section II, it can be inferred that under the MED state, stage I follows a circular trajectory, while stage II exhibits an elliptical trajectory. I_{Lr} at the point of intersection between these two trajectories is zero, and this intersection lies on the horizontal axis of the coordinate system. After normalization, the trajectories of stages I–V are centered around (10), thus the radius of stage I is equivalent to the semimajor axis of stage II. The radius ρ_{0-1} of stage I and the semimajor axis ρ_{1-2} of stage II can be expressed as follows:

$$\rho_{0-1}=\rho_{1-2}=\left|V_{C\mathrm{rpN}}(t_1)-1\right|. \tag{24}$$

According to (7) and (8), the radius ρ_{2-3} of the trajectory for stage III and the semimajor axis ρ_{3-4} of the trajectory for stage IV can be expressed as follows:

$$\rho_{2-3}=\sqrt{\left[V_{C\mathrm{rpN}}(t_2)-1\right]^2+I_{LrN}^2(t_2)} \tag{25}$$

$$\rho_{3-4}=\sqrt{\left[V_{C\mathrm{rpN}}(t_3)-1\right]^2+\frac{I_{LrN}^2(t_3)Z_1^2}{Z_0^2}}. \tag{26}$$

By substituting ρ_{3-4} into the normalized equation of (8), the expression for $I_{LrN}(t_4)$ can be obtained

$$I_{LrN}(t_4)=\frac{Z_0}{Z_1}\sqrt{\rho_{3-4}^2-\left[V_{C\mathrm{rpN}}(t_4)-1\right]^2}. \tag{27}$$

Then the trajectory radius ρ_{4-5} of stage V can be obtained

$$\rho_{4-5}=\sqrt{\left[V_{C\mathrm{rpN}}(t_4)-1\right]^2+I_{LrN}^2(t_4)}. \tag{28}$$

Since $(V_{C\mathrm{rpN}}(t_5),I_{LrN}(t_5))$ is the intersection of stages V and VI, the trajectory radius of stage VI is equal to ρ_{0-1}, so the expression for $V_{C\mathrm{rpN}}(t_5)$ can be obtained as

$$V_{C\mathrm{rpN}}(t_5)=\frac{\left(\rho_{0-1}^2-\rho_{4-5}^2\right)}{4} \tag{29}$$

plus $V_{C\mathrm{rpN}}(t_0)=-V_{C\mathrm{rpN}}(t_5)$. At this point, the trajectory nodes of stages I–V have been calculated, and based on these nodes and the trajectory equation, the calculation angle for each stage's trajectory arc can be determined

$$\begin{cases} \theta_I(t_0)=\arccos\left[\left(V_{C\mathrm{rpN}}(t_5)+1\right)/\rho_{0-1}\right] \\ \theta_{II}(t_2)=\arccos\left[\left(V_{C\mathrm{rpN}}(t_2)-1\right)/\left(V_{C\mathrm{rpN}}(t_1)-1\right)\right] \\ \theta_{III}(t_2)=\arccos\left[\left(1-V_{C\mathrm{rpN}}(t_2)\right)/\rho_{2-3}\right] \\ \theta_{III}(t_3)=\arccos\left[\left(1-V_{C\mathrm{rpN}}(t_3)\right)/\rho_{2-3}\right] \\ \theta_{IV}(t_3)=\arccos\left[\left(1-V_{C\mathrm{rpN}}(t_3)\right)/\rho_{3-4}\right] \\ \theta_{IV}(t_4)=\arccos\left[\left(1-V_{C\mathrm{rpN}}(t_4)\right)/\rho_{3-4}\right] \\ \theta_V(t_4)=\arccos\left[\left(1-V_{C\mathrm{rpN}}(t_4)\right)/\rho_{4-5}\right] \\ \theta_V(t_5)=\arccos\left[\left(1-V_{C\mathrm{rpN}}(t_5)\right)/\rho_{4-5}\right]. \end{cases} \tag{30}$$

The subscript of θ in (30) is the corresponding stage, for instance, and $\theta_1(t_0)$ is the calculation angle associated with the state trajectory of stage I at time t_0.

The complete state trajectory of the *LCC* resonant converter under the MED state can be plotted based on (24), (25), (26), (28), and (30) since the state trajectories of stages VI–X and stages I–V exhibit symmetry relative to the origin. According to the periodicity of state trajectory, a relation is established

$$\begin{aligned} \frac{T_{\mathrm{sw}}}{2}=&\sqrt{L_rC_r}\left[\theta_I(t_0)+\theta_{III}(t_3)-\theta_{III}(t_2)\right. \\ &\left.+\theta_V(t_5)-\theta_V(t_4)\right] \\ &+\sqrt{\frac{L_rC_rC_p}{C_r+C_p}}\left[\theta_{II}(t_2)+\theta_{IV}(t_4)-\theta_{IV}(t_3)\right]=\frac{1}{2f_{\mathrm{sw}}}. \end{aligned} \tag{31}$$

After substituting (23)–(30), (31) can be rewritten as a function with constants C_{r}, C_{p}, L_{r}, V_{in}, V_{o}, and n, dependent variable I_{o}, and independent variables f_{sw} and t_{rel}. The relation between t_{rel} and α_{abs} can be obtained from Fig. 6 and (30)

$$\alpha_{\mathrm{abs}}=2\pi f_{\mathrm{sw}}\left[t_{\mathrm{rel}}+\sqrt{L_rC_r}\cdot\theta_I(t_0)+\sqrt{\frac{L_rC_rC_p}{C_r+C_p}}\cdot\theta_{II}(t_2)\right]. \tag{32}$$

By replacing t_{rel} in (31) with α_{abs}, the theoretical model of the *LCC* resonant converter under the MED state can be derived.

B. AED Operating State

The *LCC* resonant converter will operate in the AED state when SF exceeds f_Q, or when SSPSA is greater than α_Q and less than π. By analogy with the state trajectory derivation process of MED state, the normalized trajectory node solution equations

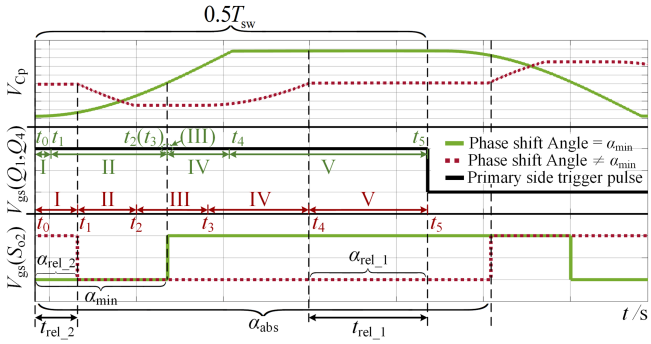

Fig. 7. Analysis of SSPSA under LED state.

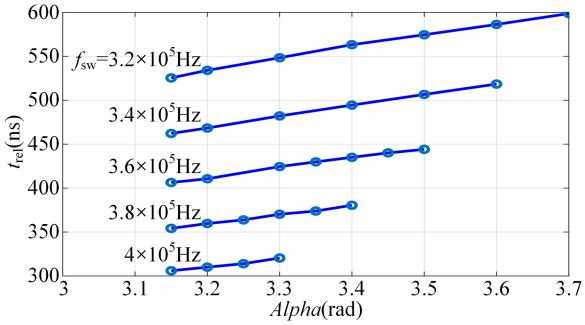

Fig. 8. Relation between $t_{\rm rel}$ and α under LED state.

of AED state are directly given as

$$\begin{cases} V_{C\rm rpN}(t_2)-V_{C\rm rpN}(t_1)=-\frac{nI_o}{2C_r f_{\rm sw}V_{\rm in}} \\ V_{C\rm rpN}(t_3)-V_{C\rm rpN}(t_2)=\frac{C_pV_o}{nC_rV_{\rm in}}+V_o/n \\ -V_{C\rm rpN}(t_1)-V_{C\rm rpN}(t_4)=\frac{C_pV_o}{nC_rV_{\rm in}}+V_o/n \\ V_{C\rm rpN}(t_4)-1=I_{LrN}(t_3)\sin(\omega_0 t_{\rm rel}) \\ \qquad\qquad +[V_{C\rm rpN}(t_3)-1]\cos(\omega_0 t_{\rm rel}) \\ I_{LrN}(t_4)=I_{LrN}(t_3)\cos(\omega_0 t_{\rm rel}) \\ \qquad\qquad -[V_{C\rm rpN}(t_3)-1]\sin(\omega_0 t_{\rm rel}) \\ I_{LrN}^2(t_3)\frac{Z_1^2}{Z_0^2}+[V_{C\rm rpN}(t_3)-1]^2=[V_{C\rm rpN}(t_2)-1]^2. \end{cases} \tag{33}$$

The trajectory parameters and the calculation angle of the trajectory arc are determined based on the trajectory node, and by exploiting the periodicity of state trajectories, the following equation can be derived:

$$\begin{aligned} \frac{T_{\rm sw}}{2}=&\sqrt{\frac{L_rC_rC_p}{C_r+C_p}}\left[\theta_I(t_0)-\theta_I(t_1)+\theta_{III}(t_3)\right. \\ &\left.+\theta_V(t_5)-\theta_V(t_4)\right] \\ &+\sqrt{L_rC_r}\left[\theta_{II}(t_1)+\theta_{IV}(t_4)-\theta_{IV}(t_3)\right]=\frac{1}{2f_{\rm sw}}. \end{aligned} \tag{34}$$

In Fig. 3(b), the relation between $t_{\rm rel}$ and $\alpha_{\rm abs}$ is as follows:

$$\begin{aligned} \alpha_{\rm abs}=2\pi f_{\rm sw}\Bigg\{&t_{\rm rel}+\sqrt{L_rC_r}\cdot\theta_{II}(t_1) \\ &+\sqrt{\frac{L_rC_rC_p}{C_r+C_p}}\cdot\left[\theta_I(t_0)-\theta_I(t_1)+\theta_{III}(t_3)\right]\Bigg\}. \end{aligned} \tag{35}$$

By replacing $t_{\rm rel}$ in (34) with $\alpha_{\rm abs}$, the theoretical model of the *LCC* resonant converter under the AED state can be derived.

C. LED Operating State

LCC resonant converter will enter LED state when $\alpha_{\rm abs}>\pi$. Different from the previous two operating states, the short-circuit state of $C_{\rm p}$ under LED state is divided into two stages, such as stage I and stage V in Fig. 7. Here, the durations of stage V and I are defined as $t_{\rm rel\_1}$ and $t_{\rm rel\_2}$, and the normalized equations for solving trajectory nodes can be derived as

$$\begin{cases} V_{C\rm rpN}(t_3)-V_{C\rm rpN}(t_2)=-\frac{nI_o}{2C_r f_{\rm sw}V_{\rm in}} \\ V_{C\rm rpN}(t_1)-V_{C\rm rpN}(t_2)=\frac{C_pV_o}{nC_rV_{\rm in}}+V_o/n \\ V_{C\rm rpN}(t_4)-V_{C\rm rpN}(t_3)=\frac{C_pV_o}{nC_rV_{\rm in}}+V_o/n \\ V_{C\rm rpN}(t_5)=I_{LrN}(t_4)\sin(\omega_0 t_{rel\_1})+ \\ [V_{C\rm rpN}(t_4)-1]\cos(\omega_0 t_{rel\_1})+1 \\ I_{LrN}(t_5)=I_{LrN}(t_4)\cos(\omega_0 t_{rel\_1})-[V_{C\rm rpN}(t_4)-1] \\ \qquad \sin(\omega_0 t_{rel\_1}) \\ V_{C\rm rpN}(t_1)=-I_{LrN}(t_5)\sin(\omega_0 t_{rel\_2})- \\ [V_{C\rm rpN}(t_5)+1]\cos(\omega_0 t_{rel\_2})+1 \\ I_{LrN}(t_1)=-I_{LrN}(t_5)\cos(\omega_0 t_{rel\_2}) \\ \qquad +[V_{C\rm rpN}(t_5)+1]\sin(\omega_0 t_{rel\_2}) \\ I_{LrN}^2(t_4)\frac{Z_1^2}{Z_0^2}+[V_{C\rm rpN}(t_4)-1]^2=[V_{C\rm rpN}(t_3)-1]^2. \end{cases} \tag{36}$$

The duration of $C_{\rm p}$ short-circuit state under LED state is $t_{\rm rel}=t_{\rm rel\_1}+t_{\rm rel\_2}$, as indicated in Fig. 7, while $\alpha_{\rm abs}$ satisfies $\alpha_{abs}=\pi+2\pi t_{rel\_2}\cdot f_{\rm sw}$. Specifically, the complex implicit transcendental equation expressing the coupling relation between $t_{\rm rel\_1}$ and $t_{\rm rel\_2}$ prevents substituting $t_{\rm rel}$ with $\alpha_{\rm abs}$ under LED state. Furthermore, the direct solution cannot deduce the theoretical relation model between $I_{\rm o}$ and $\alpha_{\rm abs}$.

The relation curve shown in Fig. 8 can be obtained through a large number of simulation data. The relation between $t_{\rm rel}$ and $\alpha_{\rm abs}$ in the LED state is approximately linear. Moreover, the curves under different SF are basically parallel to each other, so the influence of SF changes on the slope can be ignored. Therefore, the relation between $t_{\rm rel}$ and $\alpha_{\rm abs}$ is postulated as follows in this article:

$$t_{\rm rel}=t_{rel\_1}+t_{rel\_2}=k\alpha_{\rm abs}+b \tag{37}$$

where k and b are undetermined coefficients. The intersection point of the state trajectory of LED and AED states should be considered, where $\alpha_{\rm abs}=\alpha_{\rm st}=\pi$ and $t_{\rm rel}=t_{\rm rel\_st}=t_{\rm rel\_1}$ and $t_{\rm rel\_2}=0$. Consequently, the value of $t_{\rm rel\_st}$ can be determined by employing the theoretical model of AED state. Under the LED state, as $\alpha_{\rm abs}$ continues to increase, the duration of stage III will eventually diminish to zero. During this time, $I_{\rm o}$ becomes zero

and the energy solely circulates within the resonant tank without being transferred to the output side. Consequently, the waveform of half a switching cycle in the resonant tank becomes completely symmetrical, leading to an equivalence between $t_{\mathrm{rel\_1}}$ and $t_{\mathrm{rel\_2}}$. In other words, the maximum phase-shift angle $\alpha_{\max}$ of LED state corresponds to $I_{\mathrm{o}} = 0$, $t_{\mathrm{rel\_1}} = t_{\mathrm{rel\_2}} = 0.5t_{\mathrm{rel\_end}}$, and $\alpha_{abs} = \alpha_{end} = \pi + 2\pi t_{rel\_end} \cdot f_{\mathrm{sw}}$. By considering these conditions, each trajectory node can be solved, and subsequently, the calculation angle of each trajectory arc can be determined, leading to the acquisition of the value of $t_{\mathrm{rel\_end}}$

$$t_{rel\_end} = 2\sqrt{\frac{L_r C_r C_p}{C_r + C_p}}\left[\theta_{II}(t_1) - \theta_{II}(t_2) + \theta_{IV}(t_4)\right] - \frac{1}{f_{\mathrm{sw}}} + 2\sqrt{L_r C_r}\left[2\theta_I(t_0) - 2\theta_I(t_1) + \theta_{III}(t_2) + \theta_V(t_5) - \theta_V(t_4)\right]. \tag{38}$$

The substitution of $(\alpha_{st}, t_{rel\_st})$ and $(\alpha_{end}, t_{rel\_end})$ into (37) results in

$$\begin{cases} t_{rel\_st} = k\pi + b \\ t_{rel\_end} = \frac{k\pi + b}{1 - 2\pi k f_{\mathrm{sw}}}. \end{cases} \tag{39}$$

By calculating the values of k and b and substituting them into (36), the theoretical model of the *LCC* resonant converter under the LED state can be derived using the same methodology as in the previous two operating states.

D. Boundary Calculation for Each Operating State

1) Operating state transition point Q_{f}: While maintaining $t_{\mathrm{rel}} = 0$, the duration of stage V in MED state gradually decreases to 0 and transitions into AED state as SF of *LCC* resonant converter increases. At the critical point of this transition, $V_{C\mathrm{rpN}}(t_4) = V_{C\mathrm{rpN}}(t_5)$ is observed. The combination of (29) and $V_{C\mathrm{rpN}}(t_4)$ results in the following equation:

$$F_{MED-Vt4} = \frac{(\rho_{0-1}^2 - \rho_{4-5}^2)}{4} \text{ (under MED)}. \tag{40}$$

The equation contains only one unknown f_{sw}, and f_Q at Q_{f} can be determined by solving this equation.

1) Minimum phase-shift angle $\alpha_{\min}$: The solution to $\alpha_{\min}$ requires the consideration of two distinct situations. When SF is lower than f_Q, the minimum phase-shift operating point is in the MED state. Therefore, $\alpha_{\min}$ can be obtained by substituting $t_{\mathrm{rel}} = 0$ into (31) and (32). When SF exceeds f_Q, the minimum phase-shift operating point is in the AED state. In this scenario, $\alpha_{\min}$ can be obtained by substituting $t_{\mathrm{rel}} = 0$ into (34) and (35).
2) Operating mode transition point Q_{p}: As depicted in Fig. 4(b), the existence of Q_{p} is observed solely when SF is lower than f_Q. When operating under fixed SF, as the α_{abs} increases, the duration of stage V gradually decreases to zero under the MED state and then transitions into the AED state. In this scenario, (40) can also be derived, and f_{sw} is known. Therefore, by substituting f_{sw} into (40) and combining it with (32) to determine α_{abs}, the α_Q at Q_{p} can be obtained.
3) Maximum phase-shift angle $\alpha_{\max}$: $\alpha_{\max}$ of *LCC* resonant converter corresponds to α_{abs} at the zero output current point of the LED state, so there is $\alpha_{\max} = \alpha_{end}$.

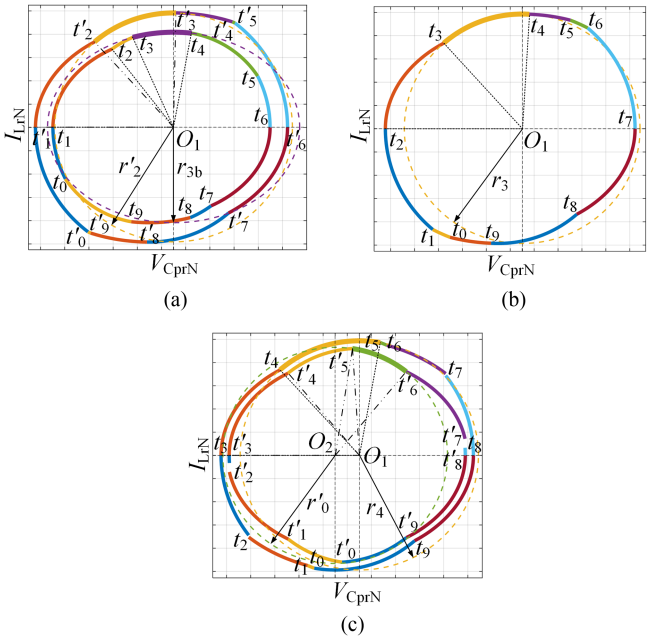

Fig. 9. Peak value of I_{Lr} when f_{sw} before the switching point $\mathrm{Q_f}$. (a) MED state. (b) AED state. (c) LED state.

IV. Control Strategy for Enhancing Transient Stability

The peak voltage and current of the resonant tank are related to the transmission efficiency and device selection, which is one of the key factors affecting the design of the *LCC* resonant converter. According to the proposed state trajectory model, the peak value of the resonant tank of VF-SSPSM *LCC* can be calculated and its characteristic curve can be drawn. Subsequently, based on the output characteristics of the converter and the peak value characteristics of the resonant tank obtained from the state trajectory model, a recommended design method of VF-SSPSM *LCC* is proposed. By analyzing the state trajectory, it is observed that the peak voltage of the resonant tank corresponds to the horizontal coordinate where the state trajectory intersects with the horizontal axis, which can be easily obtained. However, the variation in the current peak is intricate. This section focuses on the resonant current peak behavior of VF-SSPSM *LCC* under diverse operating states, followed by designing the operation range of VF-SSPSM *LCC* accordingly.

A. Before the Frequency Switch Point $\mathrm{Q_f}$

The state trajectory of an *LCC* resonant converter is depicted in Fig. 9 when f_{sw} is lower than f_Q. The state trajectories in Fig. 9(a) are both in MED state, with the α_{abs} of the trajectory in the inner ring being smaller than that of the trajectory in the outer

ring. The t_2–t_3 segment of the trajectory becomes longer and the t_4–t_5 segment becomes shorter with an increase in α_{abs}. When the central angle corresponding to the t_1–t_3 segment reaches $\angle t_1O_1t_3 \le 90°$, the peak point of I_{Lr} falls on the t_3–t_4 segment, and its peak value is equal to the semiminor axis $r_{3\text{b}}$ of the elliptical trajectory where the t_3–t_4 segment is located

$$r_{3\text{b}} = \sqrt{G^2[V_{\text{CrpN}}(t_3)-1]^2 + I_{\text{LrN}}(t_3)^2} \text{ (under MED).} \quad (41)$$

The ratio $G = \sqrt{C_{\text{p}}/(C_{\text{r}}+C_{\text{p}})}$ is the short-axis to long-axis ratio of the elliptic trajectory. When $\angle t_1O_1t_3 > 90°$, the peak point of I_{Lr} falls on segment t_2–t_3, where its value corresponds to the radius length r_2 of the circular trajectory where the t_2–t_3 segment is located

$$r_2 = \sqrt{[V_{\text{CrN}}(t_2)-1]^2 + I_{\text{LrN}}(t_2)^2} \text{ (under MED).} \quad (42)$$

The condition $r_{3\text{b}} = r_2$ is established at the point of transition between the two types of current peaks in the resonant tank under MED state. Subsequently, the transition condition can be deduced as follows:

$$\arctan\left[\frac{I_{\text{LrN}}(t_2)}{1-V_{\text{CrpN}}(t_2)}\right] + \arccos\left[\frac{1-V_{\text{CrpN}}(t_3)}{r_{3\text{b}}}\right] - \arccos\left[\frac{1-V_{\text{CrpN}}(t_2)}{r_{3\text{b}}}\right] = \frac{1}{2}\pi \text{ (under MED).} \quad (43)$$

The AED state is entered when section t_4–t_5 in Fig. 9(a) is shortened to 0. The state trajectory of the AED state is illustrated in Fig. 9(b). As the α_{abs} increases, the length of the t_5–t_6 segment gradually increases from 0 while the length of the t_4–t_5 segment gradually decreases. Throughout this process, the peak point of I_{Lr} consistently falls on the t_3–t_4 segment and corresponds to a radius length r_3 on its circular trajectory

$$r_3 = \sqrt{[V_{\text{CrpN}}(t_3)-1]^2 + I_{\text{LrN}}(t_3)^2} \text{ (under AED).} \quad (44)$$

When the t_4–t_5 segment in Fig. 9(b) is shortened to 0, the *LCC* resonant converter enters the LED state. The state trajectories in Fig. 9(c) are both in LED state, with the α_{abs} of the trajectory in the outer ring being smaller than that of the trajectory in the inner ring. When α_{abs} increases, the length of t_5–t_6 segments extends from 0, while the t_2–t_3 segments shorten. When $\angle t_3O_1t_5 \ge 90°$, the peak point of I_{Lr} occurs within the segment t_4–t_5 and corresponds to a value equal to the radius length r_4 of the circular trajectory where this segment is located

$$r_4 = \sqrt{[V_{\text{CrpN}}(t_4)-1]^2 + I_{\text{LrN}}(t_4)^2} \text{ (under LED).} \quad (45)$$

When $\angle t_3O_1t_5 < 90°$, the I_{Lr} peak value is equal to the ordinate value $I_{\text{LrN}}(t_5)$ of the state trajectory at time t_5. The condition $I_{\text{LrN}}(t_5) = r_4$ is established at the point of transition between the two types of current peaks in the resonant tank under the LED state. Subsequently, the transition condition can be deduced as follows:

$$\arctan\left[\frac{I_{\text{LrN}}(t_4)}{1-V_{\text{CrpN}}(t_4)}\right] + \arccos\left[\frac{1-V_{\text{CrpN}}(t_5)}{r_4}\right]$$

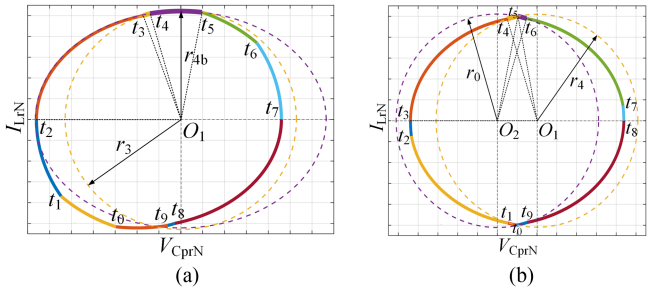

Fig. 10. Peak value of I_{Lr} when f_{sw} after the switching point Q_f. (a) AED state. (b) LED state.

$$- \arccos\left[\frac{1-V_{\text{CrpN}}(t_4)}{r_4}\right] = \frac{1}{2}\pi \text{ (under LED).} \quad (46)$$

B. *After the Frequency Switch Point* Q$_{\text{f}}$

When f_{sw} is greater than f_Q, the state trajectory of the *LCC* resonant converter is shown in Fig. 10(a), and the length of the t_3–t_4 segment increases from 0 and the t_4–t_5 segment shortens as α_{abs} increases. When $\angle t_2O_1t_5 \ge 90°$ equals zero, the peak point of I_{Lr} occurs within the segment t_4–t_5, and its value is equal to the semiminor axis $r_{4\text{b}}$ of the elliptical trajectory associated with this segment

$$r_{4\text{b}} = \sqrt{G^2[V_{\text{CrpN}}(t_4)-1]^2 + I_{\text{LrN}}(t_4)^2} \text{ (under AED).} \quad (47)$$

When $\angle t_2O_1t_5 < 90°$, the I_{Lr} peak value is equal to the ordinate value $I_{\text{LrN}}(t_5)$ of the state trajectory at time t_5. The condition $r_{4\text{b}} = I_{\text{LrN}}(t_5)$ is established at the point of transition between the two types of current peaks in the resonant tank under the AED state. Subsequently, the transition condition can be deduced as follows:

$$\arctan\left[\frac{I_{\text{LrN}}(t_3)}{1-V_{\text{CrpN}}(t_3)}\right] + \arccos\left[\frac{1-V_{\text{CrpN}}(t_4)}{r_3}\right] - \arccos\left[\frac{1-V_{\text{CrpN}}(t_3)}{r_3}\right] - \arccos\left[\frac{I_{\text{LrN}}(t_5)}{1+V_{\text{CrpN}}(t_5)}\right] - \arccos\left[\frac{I_{\text{LrN}}(t_4)}{1-V_{\text{CrpN}}(t_4)}\right] = -\frac{1}{2}\pi \text{ (under AED).} \quad (48)$$

When α_{abs} exceeds π, section t_4–t_5 in Fig. 10(a) is reduced to zero, triggering the *LCC* resonant converter to enter the LED state. The state trajectory of the LED state is illustrated in Fig. 10(b). At this time, the I_{Lr} peak value is equal to the ordinate value $I_{\text{LrN}}(t_5)$ of the state trajectory at time t_5.

The changes in the peak points of the resonant tank current for VF-SSPSM *LCC* can be summarized in Table I, as a conclusion. Based on the information provided in Section III, a phase-shifting characteristic model for the resonator current peak can be built.

TABLE I
PEAK CURRENT VALUE OF VF-SSPSM *LCC* RESONANT INDUCTOR

	MED		AED		LED	
Before Q_f	$\angle t_1O_1t_3 \le 90^\circ$	$\angle t_1O_1t_3 > 90^\circ$	r_3		$\angle t_3O_1t_5 \ge 90^\circ$	$\angle t_3O_1t_5 < 90^\circ$
	r_{3b}	r_2			r_4	$I_{LrN}(t_5)$
After Q_f			$\angle t_2O_1t_5 \ge 90^\circ$	$\angle t_2O_1t_5 < 90^\circ$	$I_{LrN}(t_5)$	
			r_{4b}	$I_{LrN}(t_5)$		

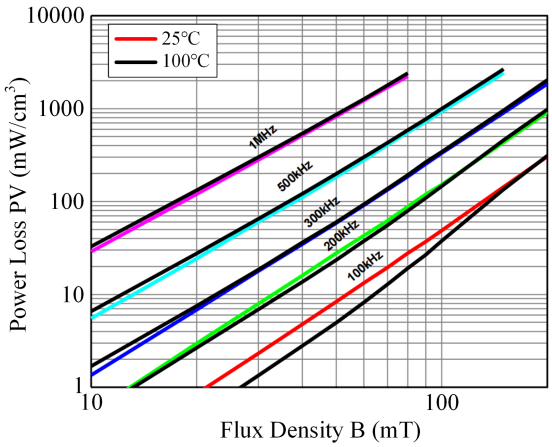

Fig. 11. DMR95 magnetic loss density curves at different frequencies.

TABLE II
STEINMETZ PARAMETERS AT DIFFERENT OPERATING FREQUENCIES

f_{sw} (kHz)	100	200	300	500	1000
κ ($\times 10^{-5}$)	3.68	2.043	1.452	1.074	1.087
α	1.8	1.8	1.81	1.81	1.82
β	2.988	2.65	2.559	2.346	2.345

C. Loss Analysis and Optimal Efficiency Point Calculation of *VF-SSPSM* LCC

The VF-SSPSM, in comparison to PFM, offers an additional degree of modulation freedom, resulting in a decoupling between output state and SF of *LCC* resonant converter. The energy transfer efficiency of *LCC* resonant converter can be optimized by appropriately configuring SF and SSPSA. The first step toward achieving this objective is to conduct a loss analysis of the *LCC* resonant converter.

The change of SSPSA can significantly affect SF and the peak value of current in the resonant tank under the same input and output conditions. Therefore, this article primarily focuses on discussing the losses incurred by magnetic components and power semiconductors as follows.

1) Magnetic Components: The magnetic components in VF-SSPSM *LCC* include an isolation transformer and a series resonant inductor. The magnetic core material utilized in this study is DMR95 of DMEGC company. Fig. 11 illustrates the magnetic loss density curves at different frequencies, as provided by the official data manual. By conducting nonlinear fitting on these curves, Steinmetz parameters of the material can be derived and are presented in Table II.

According to Table II, the relation between *Steinmetz* parameters and SF can be determined through nonlinear fitting. Subsequently, the core losses of the transformer ($P_{\text{core\_T}}$) and series resonant inductor ($P_{\text{core\_L}}$) are computed using the following two equations:

$$P_{\text{core\_}T} = \kappa C_T f_{\text{sw}}^{\alpha} \Delta B_{\mathbf{T}}^{\beta} \tag{49}$$

$$P_{\text{core\_}L} = \frac{1}{T_{\text{sw}}} \int_0^{T_{\text{sw}}} \kappa_i \left| \frac{dB_L}{dt} \right|^{\alpha} \cdot \Delta B_L^{\beta-\alpha} dt \tag{50}$$

where C_{T} is the core temperature coefficient, and its value is 1 when the operating temperature is 100 °C. The peak-to-peak flux density of the transformer is $\Delta B_T = V_{Cp}/(4N_p f_{\text{sw}} A_T)$, where N_{p} is the number of turns of the primary-side coil of the transformer, A_{T} is the effective sectional area of the magnetic core, and ΔB_{L} is the peak-to-peak flux density of the transformer, which is $\Delta B_L = 2L_r I_{\text{Lr\_max}}/(4N_L A_L)$, where $I_{\text{Lr\_max}}$ is the peak current of the resonant tank obtained in the previous section, N_{L} is the number of turns of the resonant inductor, and A_{L} is the effective sectional area of the resonant inductor core.

The conduction loss of the magnetic components increases significantly as the SF and the current peak of the *LCC* resonant converter increase, which is attributed to the skin effect and proximity effect when high-frequency ac signal flows through these components. The transformer conduction loss ($P_{\text{copper\_T}}$) is calculated as follows:

$$P_{\text{copper\_}T} = I_{\text{pri\_rms}}^2 R_{\text{ac\_pri}} + I_{\text{sec\_rms}}^2 R_{\text{ac\_sec}} \tag{51}$$

where $I_{\text{pri\_rms}}$ and $I_{\text{sec\_rms}}$ are the RMS values of current flowing through primary- and secondary-side windings of the transformer, and $R_{\text{ac\_pri}}$ and $R_{\text{ac\_sec}}$ are the equivalent ac resistance of primary- and secondary-side windings.

2) Power Semiconductors: Power semiconductors refer to MOSFETs and diodes in *LCC* resonant converters, and their losses mainly include conduction losses and switching losses. Since the *LCC* resonant converter can achieve zero voltage turn-ON of the primary side in the whole operating range, only conduction loss and turn-OFF loss need to be calculated for the primary-side switches. Taking MED state as an example, according to the modal analysis in Section II and Fig. 3, I_{Lr} can be approximately treated as a sine wave with frequency f_{sw} and peak $I_{\text{Lr\_max}}$, and the conduction loss from Q_1 to Q_4 ($P_{Q1\sim4\_\text{con}}$) can be calculated as follows:

$$P_{Q1\sim4\_\text{con}} = 4R_{Q\_\text{on}} \frac{\int_0^{\pi-\theta_I(t_0)} I_{\text{Lr\_max}} \sin\varphi d\varphi}{\pi} \tag{52}$$

where R_{Q_on} is the ON-resistance of Q_1–Q_4.

Moreover, since the antiparallel diode conduction of the primary side of VF-SSPSM *LCC* at Stage I, the conduction loss of the primary-side antiparallel diode ($P_{D\text{pri\_con}}$) can be calculated as follows:

$$P_{D\text{pri\_con}} = 2(V_{D\_on} + R_{D\_on}) \frac{\int_{\pi+2\pi T_{\text{off}}/T_{\text{sw}}-\theta_I(t_0)}^{\pi} I_{\text{Lr\_max}} \sin\varphi d\varphi}{\pi} \tag{53}$$

where V_{D_on} is the ON-voltage and R_{D_on} is the ON-resistance of the diode, $T_{\text{off}} = R_g Q_{gd} / V_{\text{gs,miller}}$. The four primary-side switches have the same turn-OFF loss ($P_{Q1\sim4\_\text{off}}$), so the time t_5 in Fig. 3(a) is used as a reference for calculation

$$P_{Q1\sim4\_\text{off}} = \frac{2}{3} V_{\text{in}} (|I_{Lr}(t_5)| - \frac{C_{ds} V_{\text{in}}}{T_{\text{off}}}) T_{\text{off}} f_{\text{sw}} \tag{54}$$

where C_{ds} is the drain–source capacitance of the main switches, R_g is the gate resistance, Q_{gd} is the gate–drain charge, and $V_{\text{gs,miller}}$ is the Miller plateau voltage. These parameters can be found in the official datasheet.

Due to the phase-shift modulation in the secondary side, only S_{o1} and S_{o2} have the ON–OFF action (when no synchronous rectification is performed), and zero-current turn-ON can be achieved. Therefore, the losses of the power semiconductors on the secondary side include conduction loss and turn-OFF loss of S_{o1} and S_{o2}, and diode conduction loss of S_1, S_2, S_{o1}, and S_{o2}.

Among them, the conduction loss of S_{o1} and S_{o2} ($P_{S\text{o1,o2\_con}}$) is calculated as follows:

$$P_{S_{\text{o1,o2\_con}}} = R_{S\_on} \frac{\int_{\theta_{II}(t_2)}^{\theta_{II}(t_2)+\theta_{III}(t_3)-\theta_{III}(t_2)} I_{\text{Lr\_max}} \sin\varphi d\varphi}{\pi} \tag{55}$$

where R_{S_on} is the ON-resistance of S_{o1} and S_{o2}.

The turn-OFF loss of S_{o1} and S_{o2} ($P_{S\text{o1,o2\_off}}$) is calculated as follows:

$$P_{S_{\text{o1,o2\_off}}} = \frac{1}{3} V_o \left(|I_{Lr}(t_3)| - \frac{C_{ds} V_o}{T_{\text{off}}} \right) T_{\text{off}} f_{\text{sw}}. \tag{56}$$

Finally, the diode conduction losses of S_1, S_2, S_{o1}, and S_{o2} ($P_{D\text{sec\_con}}$) are calculated as follows:

$$\begin{aligned} P_{D\text{sec\_con}} = {} & (V_{D\_on} + R_{D\_on}) \frac{\int_{\theta_{II}(t_2)}^{\theta_{II}(t_2)+\theta_{III}(t_3)-\theta_{III}(t_2)} I_{\text{Lr\_max}} \sin\varphi d\varphi}{\pi} \\ & + 2(V_{D\_on} + R_{D\_on}) \frac{\int_{\pi-\theta_I(t_0)-\theta_V(t_5)+\theta_V(t_4)}^{\pi} I_{\text{Lr\_max}} \sin\varphi d\varphi}{\pi}. \end{aligned} \tag{57}$$

The components listed in Table III are used in the *LCC* resonant converter designed in this article, and other parameters are given in Table IV. Combined with the state trajectory model and loss calculation formulas of the *LCC* resonant converter, the mathematical relation between the power loss and SF and SSPSA of the *LCC* resonant converter can be derived according to the parameters in Table IV and the official datasheet. According to the mathematical relation, SF and SSPSA that match the minimum power loss under a given output current target can be calculated.

TABLE III
COMPONENTS USED IN THE EXPERIMENTAL CIRCUIT

Component	Description
Resonant inductor L_r	PQ2625 Material DMR95(DMEGC)
Power transformer	PQ3230 Material DMR95(DMEGC)
DSP	TMS320F28335
Power Transistor	STWA30N65DM6AG
Gate driver	1ED40|12AFXUMA1

TABLE IV
CIRCUIT PARAMETERS OF MICROCONVERTER PROTOTYPE

Description	Symbol	Parameter
Resonant inductor	L_r	10 μH
Series resonant capacitor	C_r	29.7 nF
Parallel resonant capacitor	C_p	24.3 nF
Transformer	T	1:4
Output capacitor	C_o	0.82 μF
Input capacitor	C_{in}	0.2 μF

The curves in Fig. 12 depict the calculated power loss of VF-SSPSM *LCC* as a function of SF and SSPSA, where different curves represent different output current conditions. In this figure, there are eight loss curves from $I_o = 0.1$ A to $I_o = 1.5$ A in total, and two operating points are marked on each curve. The operating points marked by blue characters adopt traditional PFM (PFM point). PFM points on different loss curves are projected onto the *ZX* plane to be connected into blue dashed lines in the figure. The operating points marked by red characters are the operating points with the lowest calculated power loss (LCPL point). LCPL points on different loss curves are projected onto the *ZX* plane to be connected into red dashed lines in Fig. 12. Under the same output current condition, the calculated power loss of points on the red dotted line is lower than that of the points on the blue dotted line. For more intuition, Fig. 13 is plotted according to Fig. 12. In Fig. 13(a), the blue and red dotted lines depict the relation between the calculated power loss and the output current when the *LCC* resonant converter operates at PFM point and LCPL point, respectively. The efficiency curve in Fig. 13(b) is calculated based on the data presented in Fig. 13(a). It is evident that the LCPL point exhibits higher efficiency when the output current is the same.

D. *Efficiency Optimization Strategy for VF-SSPSM* LCC *With PV Panel*

In this section, based on the VF-SSPSM method and efficiency calculation in the previous section, a simple efficiency optimization control method based on the LCPL point is proposed. The control method can improve the efficiency of VF-SSPSM *LCC* with the PV panel and shorten the time of the transient process when the PV panel status changes.

In order to facilitate the verification of the proposed optimization strategy, the perturbation and observation method is used to

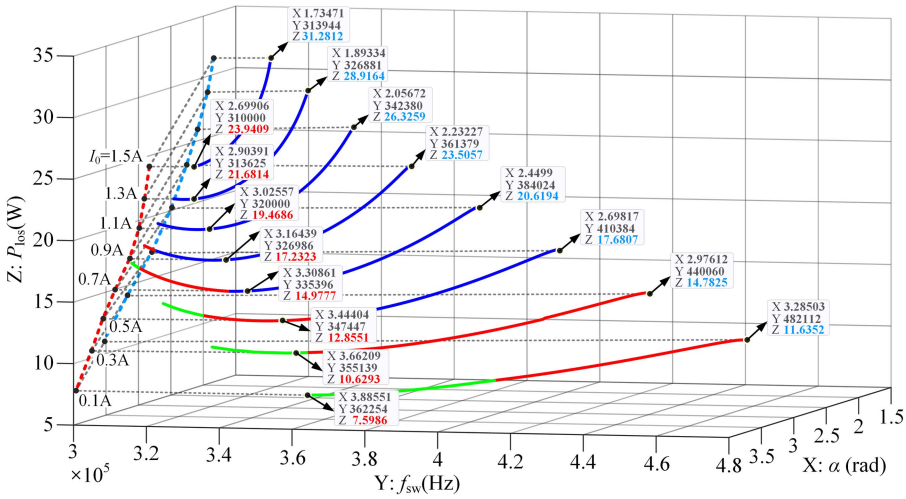

Fig. 12. Curves of the calculated power losses of *LCC* resonant converter as a function of SF and SSPSA under different output current conditions.

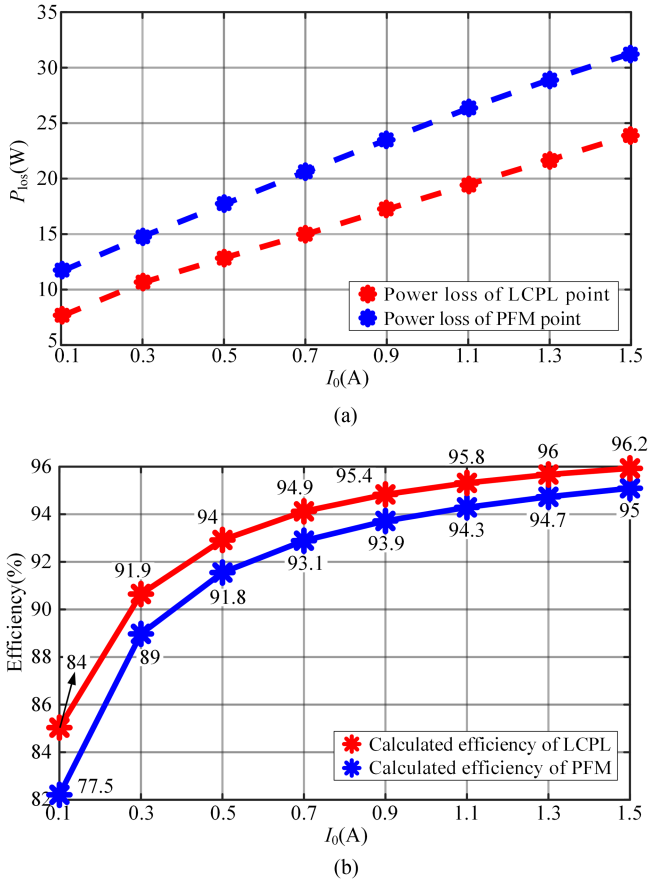

Fig. 13. Loss and efficiency curve of the VF-SSPSM *LCC* control method. (a) Loss curve. (b) Efficiency curve.

realize PV MPPT. Considering the particularity of the PV panel, when the PV panel output voltage and current are determined, the output current of the microconverter is also uniquely determined. In this case, each SF must uniquely correspond to an SSPSA. Therefore, according to a pair of matching SF and SSPSA

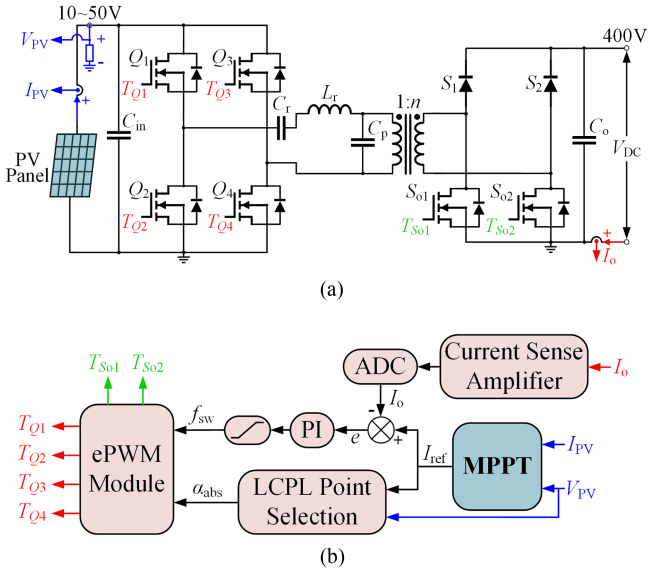

Fig. 14. Control block diagram of the VF-SSPSM *LCC* control method. (a) Power circuit. (b) Control block.

calculated in advance to maximize the efficiency, as long as SSPSA is set to the calculated value and SF is controlled through an output current closed-loop, SF will inevitably stabilize at the theoretically calculated value.

The designed efficiency optimization control method shown in Fig. 14 includes five steps as follows.

Step 1: The MPPT module executes the MPPT algorithm to obtain the reference output current $I_{\rm ref}$ of the *LCC* resonant converter.

Step 2: $f_{\rm sw}$ is regulated by a PI controller to stabilize output current $I_{\rm o}$ of LCC resonant converter at $I_{\rm ref}$. The transfer function of the PI link used in this article is as follows:

$$f_{\rm sw} = \frac{F_{\rm initial}}{(I_{ref} - I_o) \cdot (K_p + K_i \frac{1}{s}) + I_{\rm initial}} \tag{58}$$

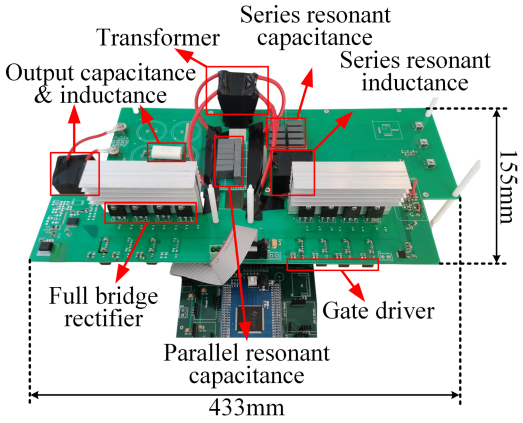

Fig. 15. Prototype board of designed *LCC* converter with an *LC* output filter.

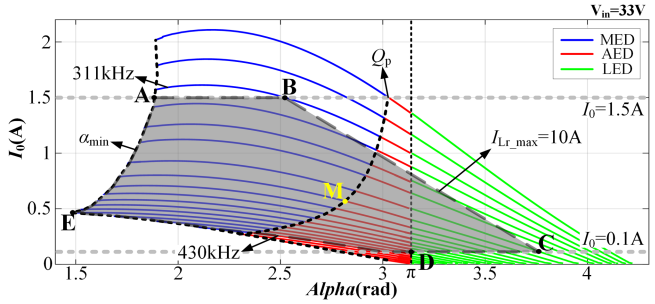

Fig. 16. Operation range of the microconverter prototype.

where $F_{\text{initial}} = 380\,000$, $K_{\text{p}} = 0.113$, $K_{\text{i}} = 427$, and $I_{\text{initial}} = 0.869$.

Step 3: The MPPT algorithm module determines whether the PV panel MPP has been reached. If so, proceed to Step 4. If not, go back to Step 1 and continue with MPPT.

Step 4: When the value of I_{o} has been stabilized at I_{ref}, the closest LCPL point is determined according to the PV panel port voltage VPV and I_{o} at this time, and the given value of α_{abs} is reset according to the LCPL point. Then f_{sw} is adjusted by PI and a new steady state is entered.

Step 5: When the change of PV output is within the specified threshold, the current state will be maintained. When the PV output situation changes beyond the specified threshold, a new round of MPPT will be carried out from Step 1.

V. Experimental Verification

A. Model Accuracy Validation

In this section, a PV microconverter prototype based on VF-SSPSM *LCC* is designed. By modeling this prototype, the accuracy of the proposed theoretical model is verified. The input of the microconverter prototype is connected to a PV panel with port voltage varying from 10 to 50 V, and the output is connected to a 400 V DC bus. The prototype's parameters are designed to ensure an output current range of 0.1–1.5 A, and an SF below 430 kHz, a resonant tank voltage peak below 190 V, and a resonant tank current peak below 10 A. The parameters of the resonant tank component, the isolation transformer ratio, and the output filter component are designed in Table IV. According to the component parameters, the designed microconverter prototype is shown in Fig. 15.

The input voltage is set at a fixed value of 33 V in this section to validate the accuracy of the theoretical model. Fig. 16 illustrates the output current characteristic curve plotted based on the model, wherein six specific operating points are designated and their coordinates are provided as follows: A(1.8987,1.5)[314 kHz], B(2.5225,1.5)[311 kHz], C(3.783,0.1)[319 kHz], D(π,0.1)[385 kHz], E(1.48,0.463)[393 kHz], and M(2.812,0.575)[340 kHz]. Among them, the f_{min}, which is 311 kHz, is achieved at point B. The α_{min} is achieved at point E, which is 1.48 rad. The α_{max} is achieved at point C, which is 3.783 rad. Point D is the state switching point of AED and LED at 385 kHz and point M is the state switching point of MED and AED at 340 kHz. The proposed theoretical model in this article is validated by conducting experiments at points A, B, C, D, E, and M. The waveforms of resonant tank voltage, current, output current, and switching voltage are observed during stable operation to determine if they align with the predefined conditions.

In Fig. 17(a), when the microconverter prototype is operating at point A, α_{abs} is set to the minimum value of 1.8987 rad at 314 kHz in the shaded region. At this operating point, α_{rel} is 0 rad, the microconverter prototype operates in MED state, and the actual output current I_0 reaches the maximum of 1.495 A, which is basically consistent with the theoretical calculation result. When turning OFF the primary side switch Q_2, the parallel resonant capacitor C_{p} is in a clamped state, as shown by point S marked in Fig. 17(a).

In Fig. 17(b), the microconverter prototype operates at point B with f_{sw} set to a minimum of 311 kHz in the shaded region. At this operating point, the microconverter prototype operates in MED state too, and the actual peak voltage of the resonant tank reaches the maximum value of 191 V, which is consistent with the theoretical calculation result. The actual output current I_0 is 1.497 A, and the percentage error with the theoretical calculation result is 0.2%.

In Fig. 17(c), the microconverter prototype operates at point C and α_{abs} is set to a maximum of 3.783 rad in the shaded region. At this time, the microconverter prototype operates in the LED state, and the actual peak current of the resonant tank reaches the maximum value of 10.1 A. The actual output current I_0 is 0.103 A, which is slightly larger than the theoretical calculation result 0.1 A. As shown by point S in Fig. 17(c), when turning OFF the primary side switch Q_2, C_{p} is in the short-circuited state, and point S divides the relative phase-shift angle into two parts: $\alpha_{\text{rel\_1}}$ and $\alpha_{\text{rel\_2}}$.

In Fig. 17(d), the microconverter prototype operates at point D with α_{abs} set to π. Referring to Fig. 16, it can be observed that at this operating point, the microconverter prototype is positioned at the switching critical point between LED and AED states. Notably, point S coincides with the termination of a short-circuit state in the parallel resonant capacitor and marks the initiation

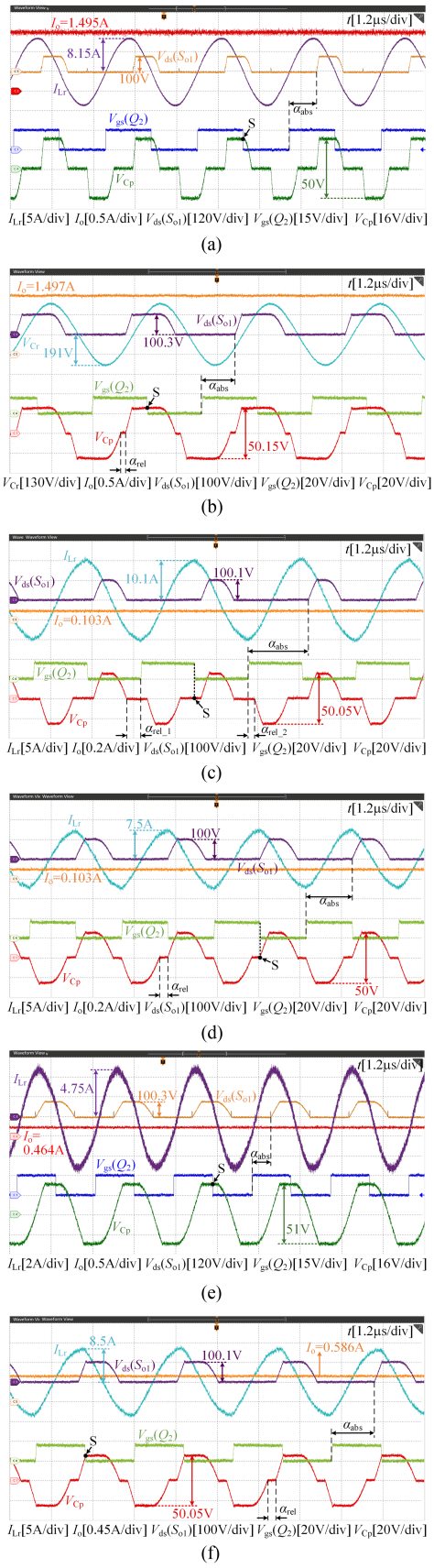

Fig. 17. Measurement waveform of microconverter prototype at different vertices. (a) Point A. (b) Point B. (c) Point C. (d) Point D. (e) Point E. (f) Point M.

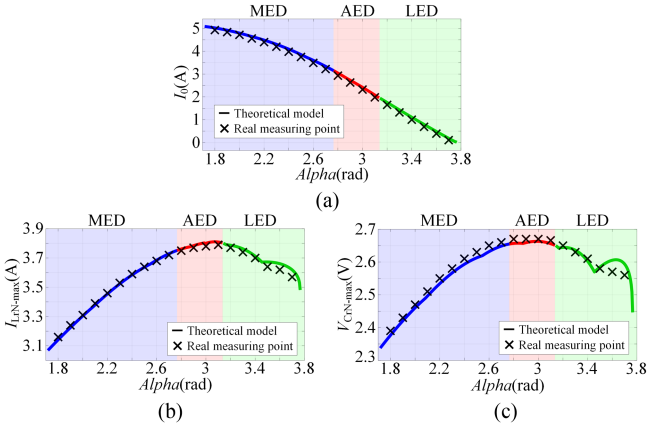

Fig. 18. Comparison of theoretical curve and measurement results under all operating states. (a) Output current. (b) Peak value of resonant tank current. (c) Peak value of resonant tank voltage.

of the charging process. The actual output current I_0 at point D measures 0.103 A, and the percentage error with the theoretical calculation result is 3%.

In Fig. 17(e), the microconverter prototype operates at point E with a maximum SF $f_{\rm sw}$ of 393 kHz and an $\alpha_{\rm abs}$ set to 1.48 rad. Within the shaded region, the microconverter prototype reaches its minimum resonant tank peak voltage and current at point E, and $\alpha_{\rm rel}$ is 0 rad. The actual output current I_0 at point E is negligibly different from the theoretical calculation result of 0.463 A, measuring at 0.464 A. The actual peak voltage and current of the resonant tank closely align with their respective theoretical calculation results, measuring at 153 V and 4.75 A.

The microconverter prototype in Fig. 17(f) operates at point M with an $f_{\rm sw}$ of 340 kHz and an $\alpha_{\rm abs}$ set to 2.812 rad. Based on Fig. 16, it can be observed that this point is the critical transition between MED and AED states. As depicted in Fig. 17(f), at point S, the parallel resonant capacitor has just completed charging and entered the clamped state.

According to the above experimental results, the vertices and critical points calculated based on the proposed model are consistent with the actual measurement results. Subsequently, a comprehensive analysis is conducted to scrutinize the error between theoretical calculations and experimental measurements.

In Fig. 18, the theoretical phase-shift characteristic curves of normalized output current I_0, resonant tank current peak $\hat{I}_{LrN}$, and voltage peak $\hat{V}_{CrN}$ under three operating states when $f_{\rm sw} =$ 325 kHz are compared with the actual measurement results of the microconverter prototype. The average error of each data under different operating states is recorded in Table V. For the output current characteristic curve, the phase-shift error is calculated. The actually measured phase-shift angle $\alpha_{\rm ps}$ and the theoretically calculated phase-shift angle $\alpha_{\rm ts}$ at each measuring point of the microconverter prototype in Fig. 18(a) are recorded, and the relative percentage error between $\alpha_{\rm ps}$ and $\alpha_{\rm ts}$ can be defined as follows:

$$\text{error} = \frac{|\alpha_{ps} - \alpha_{ts}|}{\alpha_{ps}} \times 100\%. \tag{59}$$

TABLE V
AVERAGE ERROR BETWEEN THEORETICAL CALCULATION AND EXPERIMENTAL MEASUREMENT RESULTS

	MED	AED	LED
I_0/A	2.47%	1.08%	0.967%
$I_{\text{Lr-max}}$/A	0.21%	0.41%	0.77%
$V_{\text{Cr-max}}$/V	0.54%	0.38%	0.62%

For the peak value characteristic curve of the resonant tank, the error of peak voltage and current is calculated. The actual measured current(voltage) peak $\hat{I}_{Lr-ps}(\hat{V}_{Cr-ps})$ and the theoretically calculated current(voltage) peak $\hat{I}_{Lr-ts}(\hat{V}_{Cr-ts})$ at each measuring point of the microconverter prototype in Fig. 18(b) and (c) are recorded, and the relative percentage error can be defined as follows:

$$\text{error} = \frac{\left|\hat{I}_{Lr-ps} - \hat{I}_{Lr-ts}\right|}{\hat{I}_{Lr-ps}} \times 100\% \tag{60}$$

$$\text{error} = \frac{\left|\hat{V}_{Cr-ps} - \hat{V}_{Cr-ts}\right|}{\hat{V}_{Cr-ps}} \times 100\%. \tag{61}$$

The relative percentage error is computed at all measuring points, and the average error for each operating state is separately calculated, as illustrated in Table V.

Combined with Fig. 18 and Table V, it shows good consistency between the microconverter prototype and theoretical model under all operating states. The proposed model in this article not only achieves an average error of less than 5% under all operating states but also accounts for states with SSPSM. Compared to the *LCC* resonant converter model in [36], [37], and [38], the accuracy and applicability have been significantly improved. It is worth noting that the model is capable of accurately predicting the peak values of voltage and current in the *LCC* resonant tank, with an average percentage error of less than 1% under all operating states, which helps to accurately calculate the losses. Even under light load conditions, the error does not increase significantly.

Furthermore, as the output current decreases, the relative percentage error displays a decreasing trend. The proposed state trajectory model, therefore, has good accuracy under various operating conditions, which is helpful for the high-precision design of *LCC* resonant converter.

B. High Step-Up Wide Range PV Generation Experimental Verification

Two PV *I–V* curves are plotted in Fig. 19. Here, the solid curve is the PV *I–V* curve of the series PV panel under irradiance of 1000 W/m^2, and the dotted curve is the PV *I–V* curve of the parallel PV panel under irradiance of 250 W/m^2. It can be seen that the MPP of the solid curve has $V_{\text{PV}} = 33$ V and $I_{\text{PV}} = 9.21$ A, and the MPP of the dotted curve has $V_{\text{PV}} = 15$ V and $I_{\text{PV}} = 4.2$ A. PV microconverter prototype is controlled to reach two MPPs respectively, and the measurement results are as follows.

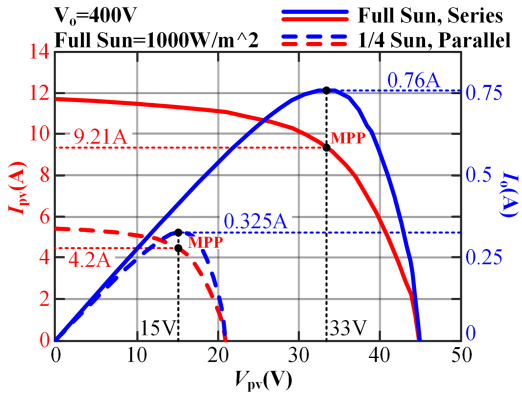

Fig. 19. PV *I–V* curves under different connection modes and light intensities.

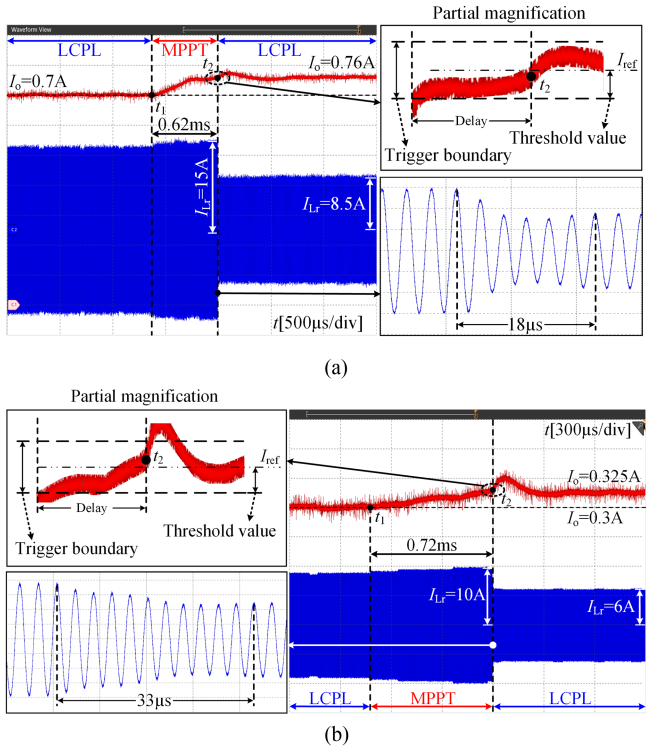

Fig. 20. PV microconverter implements LCPL mode at MPP under different PV panel operating conditions. (a) Irradiance of 1000 W/m^2, series. (b) Irradiance of 250 W/m^2, parallel.

In Fig. 20(a), the series PV panel works under irradiance of 1000 W/m^2. Before t_1, I_0 is stable at 0.7 A. At t_1, $I_{\text{ref}} = 0.76$ A is given, and at t_2, I_0 reaches the trigger threshold. At this time, the PV panel reaches MPP under the present condition and the microconverter switches to LCPL mode with $V_{\text{in}} = 33$ V and $I_0 = 0.76$ A. In Fig. 20(b), the parallel PV panel works under irradiance of 250 W/m^2. Before t_1, I_0 is stable at 0.3 A. At t_1, $I_{\text{ref}} = 0.325$ A is given, and at t_2, I_0 reaches the trigger threshold. At this time, the PV panel reaches MPP under the present condition and the microconverter switches to LCPL mode with $V_{\text{in}} = 15$ V and $I_0 = 0.325$ A.

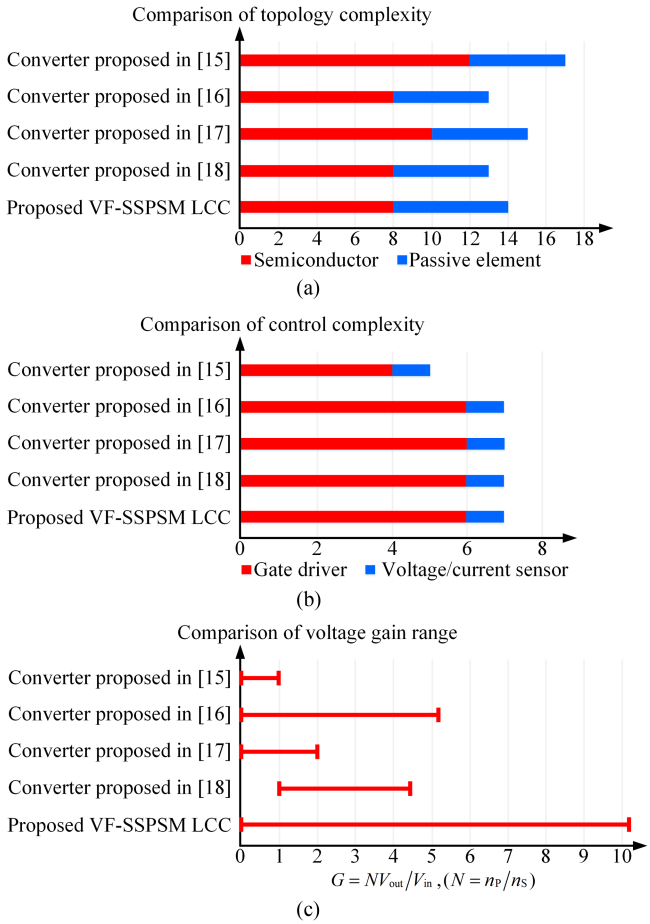

Fig. 21. Comparison between different topologies.

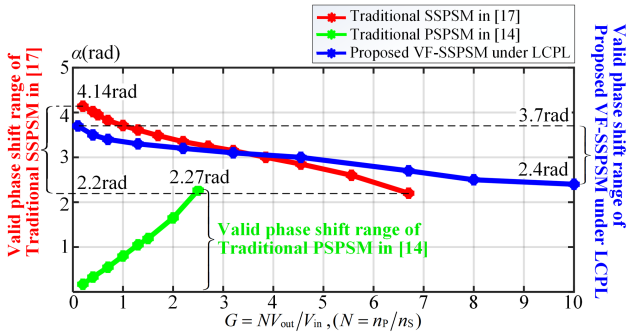

Fig. 22. Valid phase-shift range and voltage gain range comparison between different modulation strategies.

As in Fig. 20, when I_{ref} given by the MPPT algorithm changes at t_1, I_{o} of PV microconverter is controlled to track I_{ref}. After I_{o} enters the trigger boundary and after a certain time delay, the PV microconverter switches LCPL mode at t_2. Subsequently, I_{o} again tracks I_{ref} and stabilizes within the trigger boundary until the next MPPT behavior occurs.

It can be seen that the PV microconverter designed in this section can achieve MPPT under both series PV panel irradiance of 1000 W/m^2 and parallel PV panel irradiance of 250 W/m^2. The port voltage adjustment range of the PV panel covers 10–50 V, and the maximum voltage gain reaches 40× (the net gain without a transformer is ten times). Moreover, it can be seen from Fig. 20 that after switching to LCPL mode, the amplitude of I_{Lr} is significantly reduced, which can improve the efficiency of the microconverter at MPP.

C. LCPL Point-Based Efficiency Optimization Control

To compare the performance of the proposed VF-SSPSM under LCPL and existing methods, several traditional modulation strategies and the methods proposed in [14], [15], [16], and [17] are implemented to perform some additional tests on the *LCC* prototype, respectively.

In Fig. 21, the topology complexity, control complexity, and voltage gain range of the proposed VF-SSPSM *LCC* converter are compared with those proposed in several references. Among them, Altin et al. [14] combined PSPSM and PFM to optimize the efficiency of the *LLC* resonant converter but it is for buck application scenarios. The authors in [15], [16], and [17] adopted SSPSM with fixed frequency to modulate *LLC* resonant converters. In Table VI, the performance of various modulation strategies is compared for wide gain range applications. Combining Table VI and Fig. 21, the proposed VF-SSPSM *LCC* has obvious advantages in the voltage gain range and soft-switching range despite its ordinary circuit complexity, control complexity, and application range.

In order to further verify the advantages of the proposed method in increasing voltage gain range, it is implemented on the same prototype with traditional SSPSM and PSPSM, and the voltage gain range of three modulation strategies is compared. Fig. 22 shows the valid phase-shift range and the corresponding achievable gain range of the prototype when different modulation strategies are applied. The traditional PSPSM has a narrow voltage gain range, which cannot achieve a large voltage gain, and requires a large phase-shift angle variation range (0–2.27 rad corresponds to 0–2.5× gain). The traditional SSPSM has more than twice the voltage gain range compared to PSPSM, and the required phase-shift angle variation range is also much smaller (2.2–4.14 rad corresponds to 0–6.7× gain). The proposed VF-SSPSM under LCPL further expands the voltage gain range and requires only a smaller range of phase-shift angle variation (2.4–3.7 rad corresponding to 0–10× gain) due to the cooperation of frequency change.

Based on loss analysis, VF-SSPSM under LCPL can effectively reduce the transformer and switch conduction losses. In order to verify the theory, the input voltage of the prototype is fixed to 50 V, and the output current is adjusted. The prototype is modulated by PFM, SSPSM, PSPSM, and the proposed method, respectively, and the operating efficiency under different output currents is measured and compared. In Fig. 23, the proposed method can maintain relatively high efficiency over the whole output current range. At a small output current, the efficiency is increased by 2.3% compared with PSPSM and 5.8% compared with SSPSM. At a large output current, the efficiency is

TABLE VI
PERFORMANCE COMPARISON OF DIFFERENT MODULATION STRATEGIES FOR WIDE GAIN RANGE APPLICATION

Modulation Strategy	Gain Range	ZVS for Primary	ZVS for Secondary	Additional MOSFET	Circuit Complexity	Application Range
PFM	**Medium**	Yes	**No**	NA	Low	Very Wide
PSPWM	**Narrow**	Yes	**No**	**Two**	Medium	**Narrow**
SSPWM	**Medium**	Yes	**No**	**One**	**High**	**Narrow**
APWM	**Medium**	Yes	**No**	NA	Low	Wide
PSPSM	**Narrow**	**Limited**	**No**	NA	Low	Wide
SSPSM	**Wide**	Yes	Half	NA	Medium	Medium
Proposed VF-SSPSM	**Very Wide**	**Yes**	**Half**	**NA**	**Medium**	**Medium**

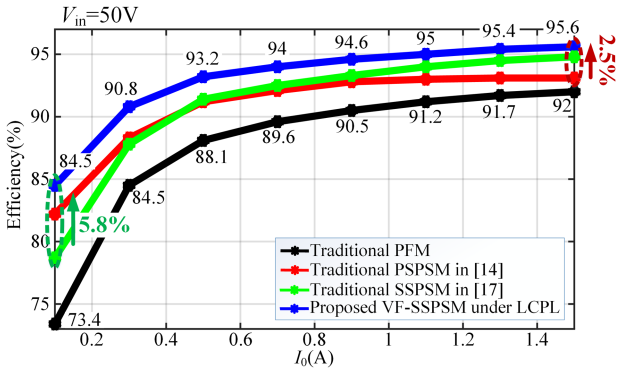

Fig. 23. Operating efficiency comparison between different modulation strategies.

increased by 2.5% compared with PSPSM and 0.6% compared with SSPSM. This is because when the input and output voltages are fixed, at a small output current, the SSPSM strategy will cause a large circulating current at the secondary side due to a large SSPSA, while the proposed method alleviates this problem by cooperating with the regulation of SF. At large output current, the efficiency of the PSPSM strategy is affected because of the large phase-shift angle and even enters the capacitive region. Therefore, the efficiency of the SSPSM strategy and the proposed method is higher than that of the PSPSM strategy at large output current. Therefore, the proposed method can improve efficiency at a small output current compared with SSPSM and can improve efficiency at a large output current compared with PSPSM.

VI. CONCLUSION

In order to design a PV microconverter with high step-up, wide gain range, and high efficiency, this article proposes an *LCC* resonant converter model covering variable-frequency and secondary-side phase-shift based on the state trajectory method. By using this model, the loss analysis of VF-SSPSM *LCC* is completed, and the efficiency optimization control method of the PV microconverter based on the LCPL point is designed. Finally, the experimental results demonstrate a consistent agreement with the theoretical design, validating all critical points designed by the theoretical model. In the MED state, the maximum percentage error of output current is 2.47%. In AED and LED states, the error is approximately 1.1%. The error of peak voltage and current of the resonant tank is less than 1% in all three states. The PV microconverter, based on VF-SSPSM *LCC*, features an adjustable input voltage range of 10–50 V and a maximum voltage gain of 40× (the net gain without transformer is ten times). Compared with SSPSM and PSPSM, the proposed method can improve the operating efficiency of the prototype by 5.8% and 2.5% at small and large output currents, respectively.

REFERENCES

[1] D. Vinnikov, A. Chub, R. Kosenko, V. Sidorov, and A. Lindvest, "Implementation of global maximum power point tracking in photovoltaic microconverters: A survey of challenges and opportunities," *IEEE J. Emerg. Sel. Topics Power Electron.*, vol. 11, no. 2, pp. 2259–2280, Apr. 2023, doi: 10.1109/JESTPE.2021.3137521.

[2] A. K. Bhattacharjee, N. Kutkut, and I. Batarseh, "Review of multiport converters for solar and energy storage integration," *IEEE Trans. Power Electron.*, vol. 34, no. 2, pp. 1431–1445, Feb. 2019, doi: 10.1109/TPEL.2018.2830788.

[3] K. Kanathipan and J. Lam, "A high voltage gain isolated PV microconverter with a single-voltage maximum power point tracking control loop for DC micro-grid systems," *IEEE J. Emerg. Sel. Topics Ind. Electron.*, vol. 3, no. 3, pp. 755–765, Jul. 2022, doi: 10.1109/JESTIE.2021.3130473.

[4] K. Kanathipan, R. Emamalipour, and J. Lam, "A single-switch high-gain PV microconverter with low-switch-voltage-to-high-voltage-bus ratio," *IEEE Trans. Power Electron.*, vol. 35, no. 9, pp. 9530–9540, Sep. 2020, doi: 10.1109/TPEL.2020.2974207.

[5] D. Sha, J. Zhang, and J. Wu, "A GaN-based microconverter utilizing fixed-frequency BCM control method for PV applications," *IEEE Trans. Ind. Electron.*, vol. 65, no. 6, pp. 4771–4780, Jun. 2018, doi: 10.1109/TIE.2017.2772159.

[6] A. Chub, D. Vinnikov, R. Kosenko, and E. Liivik, "Wide input voltage range photovoltaic microconverter with reconfigurable buck–Boost switching stage," *IEEE Trans. Ind. Electron.*, vol. 64, no. 7, pp. 5974–5983, Jul. 2017, doi: 10.1109/TIE.2016.2645891.

[7] C.-H. Kwon et al., "15-kV and 1.8-kJ/s high-precision capacitor charging power supply based on LCC resonant converter for kicker modulator system," *IEEE Trans. Plasma Sci.*, vol. 51, no. 10, pp. 2841–2848, Oct. 2023, doi: 10.1109/TPS.2023.3290968.

[8] C. Yu et al., "Solid State pulsed power modulator with high repetition rate and short pulse width for high-speed pulsed lasers," *IEEE Trans. Ind. Electron.*, vol. 71, no. 1, pp. 388–397, Jan. 2024, doi: 10.1109/TIE.2023.3241247.

[9] C. Lin, L. He, X. Li, M. Xie, L. Cheng, and S. Fan, "Modeling and digital control of 100kV/50kW high voltage power supply based on PPSS-LCC for X-ray generator," in *Proc. IEEE 4th Int. Elect. Energy Conf.*, Wuhan, China, 2021, pp. 1–6, doi: 10.1109/CIEEC50170.2021.9510975.

[10] A. Pawellek, C. Oeder, J. Stahl, and T. Duerbaum, "The resonant LLC vs. LCC resonant converter - comparing two optimized prototypes," in *Proc. IEEE Energy Convers. Congr. Expo.*, Phoenix, AZ, USA, 2011, pp. 2229–2235, doi: 10.1109/ECCE.2011.6064064.

[11] Y. Wei, Q. Luo, and H. A. Mantooth, "LLC and CLLC resonant converters based DC transformers (DCXs): Characteristics, issues, and solutions," *CPSS Trans. Power Electron. Appl.*, vol. 6, no. 4, pp. 332–348, Dec. 2021, doi: 10.24295/CPSSTPEA. 2021.00031.
[12] Y. Wei, Q. Luo, and A. Mantooth, "Overview of modulation strategies for LLC resonant converter," *IEEE Trans. Power Electron.*, vol. 35, no. 10, pp. 10423–10443, Oct. 2020, doi: 10.1109/TPEL.2020.2975392.
[13] S. Liu and F. Zhang, "State variable derivation with numerical approach and efficiency optimisation method for phase-shift LLC converters under wide voltage-gain range," *IET Power Electron*, vol. 12, no. 7, pp. 1752–1762, Jun. 2019, doi: 10.1049/iet-pel.2018.5213.
[14] N. Altin, S. Ozdemir, M. Khayamy, and A. Nasiri, "A novel topology for solar PV inverter based on an LLC resonant converter with optimal frequency and phase-shift control," *IEEE Trans. Ind. Appl.*, vol. 58, no. 4, pp. 5042–5054, Jul./Aug. 2022, doi: 10.1109/TIA.2022.3163372.
[15] H. Wu, Y. Lu, T. Mu, and Y. Xing, "A family of soft-switching DC–DC converters based on a phase-shift-controlled active boost rectifier," *IEEE Trans. Power Electron.*, vol. 30, no. 2, pp. 657–667, Feb. 2015, doi: 10.1109/TPEL.2014.2308278.
[16] H. Wu, L. Chen, and Y. Xing, "Secondary-side phase-shift-controlled dual-transformer-based asymmetrical dual-bridge converter with wide voltage gain," *IEEE Trans. Power Electron.*, vol. 30, no. 10, pp. 5381–5392, Oct. 2015, doi: 10.1109/TPEL.2014.2371922.
[17] H. Wu, T. Mu, X. Gao, and Y. Xing, "A secondary-side phase-shift-controlled LLC resonant converter with reduced conduction loss at normal operation for hold-up time compensation application," *IEEE Trans. Power Electron.*, vol. 30, no. 10, pp. 5352–5357, Oct. 2015, doi: 10.1109/TPEL.2015.2418786.
[18] A. Chub, D. Vinnikov, O. Korkh, M. Malinowski, and S. Kouro, "Ultrawide voltage gain range microconverter for integration of silicon and thin-film photovoltaic modules in DC microgrids," *IEEE Trans. Power Electron.*, vol. 36, no. 12, pp. 13763–13778, Dec. 2021, doi: 10.1109/TPEL.2021.3084918.
[19] C. Sun, Q. Sun, R. Wang, P. Zhang, L. Zhang, and P. Wang, "Universal synchronous rectification scheme for LLC resonant converter using primary-side inductor voltage," *IEEE Trans. Ind. Electron.*, vol. 70, no. 6, pp. 5747–5759, Jun. 2023, doi: 10.1109/TIE.2022.3199946.
[20] C. Sun, R. Wang, Q. Sun, and H. Zhang, "A novel synchronous rectification scheme with low computational burden for LLC resonant converter in EV charger applications," *IEEE Trans. Ind. Electron.*, vol. 70, no. 9, pp. 8991–9003, Sep. 2023, doi: 10.1109/TIE.2022.3215445.
[21] D. Li, Q. Sun, R. Wang, and Z. Sui, "Transient stability analysis and enhancement of inverter-based microgrid considering current limitation," *IEEE Trans. Power Electron.*, early access, Sep. 2024, doi: 10.1109/TPEL.2024.3467215.
[22] J.-Y. Lin, P.-H. Liu, H.-Y. Yueh, and Y.-F. Lin, "Design and analysis of LLC resonant converter with Valley switching control for light-load conditions," *IEEE J. Emerg. Sel. Topics Power Electron.*, vol. 10, no. 5, pp. 6033–6044, Oct. 2022, doi: 10.1109/JESTPE.2022.3173257.
[23] Y. Wei, Q. Luo, X. Du, N. Altin, J. M. Alonso, and H. A. Mantooth, "Analysis and design of the LLC resonant converter with variable inductor control based on time-domain Analysis," *IEEE Trans. Ind. Electron.*, vol. 67, no. 7, pp. 5432–5443, Jul. 2020, doi: 10.1109/TIE.2019.2934085.
[24] A. Awasthi, S. Bagawade, and P. K. Jain, "Analysis of a hybrid variable-frequency-duty-cycle-modulated low-Q LLC resonant converter for improving the light-load efficiency for a wide input voltage range," *IEEE Trans. Power Electron.*, vol. 36, no. 7, pp. 8476–8493, Jul. 2021, doi: 10.1109/TPEL.2020.3046560.
[25] Z. Cheng, H. Peng, J. Chen, Y. Kang, J. Wu, and X. Chu, "Resonant tank switch methodologies for narrow switching frequency range in wide output range LCC resonant converter," *IEEE J. Emerg. Sel. Topics Power Electron.*, vol. 10, no. 1, pp. 822–836, Feb. 2022, doi: 10.1109/JESTPE.2021.3102665.
[26] R. Yang, H. Ding, Y. Xu, L. Yao, and Y. Xiang, "An analytical steady-state model of LCC type series–Parallel resonant converter with capacitive output filter," *IEEE Trans. Power Electron.*, vol. 29, no. 1, pp. 328–338, Jan. 2014, doi: 10.1109/TPEL.2013.2248753.
[27] J. Liu, J. Zhang, T. Q. Zheng, and J. Yang, "A modified gain model and the corresponding design method for an LLC resonant converter," *IEEE Trans. Power Electron.*, vol. 32, no. 9, pp. 6716–6727, Sep. 2017, doi: 10.1109/TPEL.2016.2623418.
[28] W. Feng, F. C. Lee, and P. Mattavelli, "Simplified optimal trajectory control (SOTC) for LLC resonant converters," *IEEE Trans. Power Electron.*, vol. 28, no. 5, pp. 2415–2426, May 2013, doi: 10.1109/TPEL.2012.2212213.
[29] W. Feng, F. C. Lee, and P. Mattavelli, "Optimal trajectory control of burst mode for LLC resonant converter," *IEEE Trans. Power Electron.*, vol. 28, no. 1, pp. 457–466, Jan. 2013, doi: 10.1109/TPEL.2012.2200110.
[30] J. Zhao, L. Wu, and G. Chen, "Adaptive burst mode of LCC resonant converters with reduced audible noise," *IEEE Trans. Ind. Electron.*, vol. 69, no. 10, pp. 10457–10466, Oct. 2022, doi: 10.1109/TIE.2022.3163555.
[31] J. Zhao et al., "Fast and accurate control strategy for LCC resonant converters based on simplified state trajectory and two-point solution method," *IEEE Trans. Power Electron.*, vol. 37, no. 5, pp. 5309–5319, May 2022, doi: 10.1109/TPEL.2021.3133925.
[32] L. Wu, J. Zhao, H. Lin, X. Sun, and G. Chen, "State trajectory control of startup for LCC resonant converters with capacitive output filter," *IEEE J. Emerg. Sel. Topics Power Electron.*, vol. 9, no. 2, pp. 2317–2327, Apr. 2021, doi: 10.1109/JESTPE.2020.2981683.
[33] J. Zhao, L. Wu, H. Lin, X. Sun, and G. Chen, "State trajectory control of burst mode for LCC resonant converters with capacitive output filter," *IEEE Trans. Power Electron.*, vol. 37, no. 1, pp. 377–391, Jan. 2022, doi: 10.1109/TPEL.2021.3100539.
[34] Y. Xu et al., "Multimode constant power control strategy for LCC resonant capacitor charging power supply based on state plane analysis," *IEEE Trans. Power Electron.*, vol. 36, no. 7, pp. 8399–8412, Jul. 2021, doi: 10.1109/TPEL.2020.3042824.
[35] A. J. Gilbert, C. M. Bingham, D. A. Stone, and M. P. Foster, "Normalized analysis and design of LCC resonant converters," *IEEE Trans. Power Electron.*, vol. 22, no. 6, pp. 2386–2402, Nov. 2007, doi: 10.1109/TPEL.2007.909243.
[36] S. Tian, F. C. Lee, and Q. Li, "Equivalent circuit modeling of LLC resonant converter," *IEEE Trans. Power Electron.*, vol. 35, no. 8, pp. 8833–8845, Aug. 2020, doi: 10.1109/TPEL.2020.2967346.
[37] V. Sessa, L. Rubino, L. Iannelli, F. Vasca, and P. Marino, "Complementarity model for steady-state analysis of resonant LLC power converters," *IEEE Trans. Circuits Syst. II, Exp. Briefs*, vol. 66, no. 7, pp. 1182–1186, Jul. 2019, doi: 10.1109/TCSII.2018.2875591.
[38] S. Mao, C. Li, W. Li, J. Popović, S. Schröder, and J. A. Ferreira, "Unified equivalent steady-state circuit model and comprehensive design of the LCC resonant converter for HV generation architectures," *IEEE Trans. Power Electron.*, vol. 33, no. 9, pp. 7531–7544, Sep. 2018, doi: 10.1109/TPEL.2017.2774147.

Qianxiang Shen received the B.S. and M.Sc. degrees in electrical engineering in 2019 and 2022, respectively, from the School of Information Science and Engineering, Northeastern University, Shenyang, China, where he is currently working toward the Ph.D. degree in electrical engineering.

His current research interests include topology, modeling, modulation strategy of dc–dc converters, and its application in photovoltaic systems.

Qiuye Sun (Senior Member, IEEE) received the Ph.D. degree in control theory and control engineering from Northeastern University, Shenyang, China, in 2007.

He is currently a Full Professor with Northeastern University and obtained Special Government Allowances from the State Council in China. His current research interests include optimization analysis technology of power distribution networks, network control of energy Internet, integrated energy systems, and microgrids.

Enhui Chu received the M.S. degree in automation from Northeastern University, Shenyang, China, in 1993, and the Ph.D. degree in electrical engineering from Yamaguchi University, Yamaguchi, Japan, in 2002.

From 1997 to 1999, he was a Visiting Scholar and a Researcher with Yamaguchi University, Yamaguchi. From 2003 to 2006, he was a Researcher with Yutaka Electric Manufacturing Company, Ltd., Nippon Steel and Sumitomo Metal Corporation. Since 2006, he has been with the College of Information Science and Engineering, Northeastern University, Shenyang, China, where he is currently a Professor. So far, he has been working on power electronics and its applications. His research interests include power converters, medical electronics, autoelectronics, soft-switching techniques, and the application of soft-switching techniques in renewable energy power conversion systems.

Chenghao Sun (Student Member, IEEE) received the B.S. and M.Sc. degrees in electronic science and technology and the Ph.D. degree in electrical engineering from Northeastern University, Shenyang, China, in 2017, 2019, and 2023, respectively.

His current research interests include modeling, modulation strategy, and SR of resonant converters.